Journal of Biomedical Engineering and Medical Imaging

TABLE OF CONTENTS

DISCLAIMER

A New Edge Detection Method for CT-Scan Lung Images

[1]Ali El-Zaart and [2]Toufic El-Arwadi

Department of Mathematics and Computer Science, Faculty of Science,
Beirut Arab University, Lebanon

[1]elzaart@bau.edu.lb; [1]dr_elzaart@yahoo.com; [2]t.elarwadi@bau.edu.lb; [2]telarwadi@gmail.com

ABSTRACT

Lung cancer is one of the most serious health problems in the world. Lung Computer-Aided Diagnosis (CAD) is a potential method to accomplish a range of quantitative tasks such as early cancer and disease detection, analysis of disease progression. Edge detection in Lung image is a fundamental step in CAD system and many algorithms have suggested for edge detection in image. In this paper a new operator has developed for edge detection based on finite difference method. Experimentation showed that the proposed operator gave good results in detection the edges in Lung images.

Keywords: Lung image; adaptive mask; finite difference method; gradient.

[1] Introduction

L Computed tomography, more commonly known as a CT or CAT scan, is a diagnostic medical test that, like traditional x-rays, produces multiple images or pictures of the inside of the body. A chest CT Scan produces images of sufficient image quality to detect many lung diseases and abnormalities [].Because CT scans are able to detect even very small nodules in the lung, chest CT is especially effective for diagnosing lung cancer at its earliest, most curable stage [2-5]. Survival from lung cancer is directly related to its growth at its detection time. . The earlier the detection is, the higher the chances of successful treatment. Lung Computer-Aided Diagnosis (CAD) is a potential method to accomplish a range of quantitative tasks such as early cancer and disease detection, analysis of disease progression. Edge detection in Lung image is a fundamental step in CAD system and many algorithms have suggested for edge detection in image [1]. The purpose of this paper is to develop a new 5x5 operator for edge detection in Lung images. This operator is based on the finite difference method. The rest of this paper is organized as follows. Section 2 presents the related work of edge detection. Section 3 presents the proposed method. Experimental results are shown in section 4. Finally this paper presents conclusion and future work in section 5.

[2] The Existing Ranking Methods

Medical image edge detection is an important work for object recognition of the human organs such as lungs, and it is an essential pre-processing step in medical image segmentation [1]. In some applications it may be useful to classify image pixels into anatomical regions, such as bones, muscles, and blood vessels, while in others into pathological regions, such as cancer, tissue deformities and multiple sclerosis lesions. The goal of the lung edge detection required for the computer aided diagnosis from CT scan images is to

essentially separate the voxels corresponding to the lung cavity in the axial CT scan slices from the surrounding lung anatomy. Over the years, many methods have been proposed for detecting edges in images. Some of the earlier methods, such as the Sobel and Prewitt detectors used local gradient operators [1,7,8] to obtain spatial filter masks. The procedure is to compute the sum of products of the mask coefficients with the intensity values in the region encompassed by the mask [10]. In addition, the Canny edge detector which depends on the Gaussian distribution for obtaining the operators for the gradient and Laplacian masks is a well-known edge detector [10]. In this paper, we propose 5x5 masks for edge detection in Lung CT images. The method is based on the 1D and 2D Taylor's. In our previous work, the developed a 5x5 operator based on the 1D and 3D Taylor's and we obtain an operator composed of two parameters α and β, in this paper we added a third parameter on the operator in order to have more general operator than the one in [6]. In next section, we will explain the new operator.

[3] **The Modified Operators**

In this section, we will improve the operator developed in our previous work [6]. The previous operator is based on 2D Taylor expansion and we used two parameters α and β in order to construct the operators (masks). In this paper we will modify the previous operator by adding a new parameter γ. In the follows we will explain the modified operator. First in section 3.1, we will explain the 1D Taylor's formula and then in section 3.2 we will explain the 2D Taylor's expansion.

In pure mathematics, given a function $f \in C^{n+1}$ that is, all its derivatives $f^{(j)}, j = 1, \dots, n + 1$ are continuous. Let x be a fixed point, then for h close to 0, there exists $t \in (0,1)$ such that:

$$f(x + h) = f(x) + \sum_{i=1}^{n} \frac{h^i}{i!} f^{(i)}(x) + f^{(n+1)}(c) \frac{h^{n+1}}{(n + 1)!} \tag{1}$$

Where $c = x + th$. The term $R_n := f^{(n+1)}(c) \frac{h^{n+1}}{(n+1)!}$ is called the remainder term. Using the $big - O$ notation, we abbreviate the formula (1) as follow:

$$f(x + h) = f(x) + \sum_{i=1}^{n} \frac{h^i}{i!} f^{(i)}(x) + O(h^{n+1}) \tag{2}$$

Let X be a normed vector space, If $f: X \to R$ is differentiable $n + 1$ times on X, it may be expanded by Taylor's formula, for each $x \in X$:

$$f(x + h) = f(x) + Df(x).h + \frac{1}{2!} D^2 f(x).h^2 + \dots + \frac{1}{n!} D^n f(x).h^n + R_n(x) \tag{3}$$

Where $R_n(x) = \frac{1}{(n+1)!} D^{n+1} f(c).h^{n+1}$. The k-Frechet Derivative of f at x is being denoted by $D^k f(x)$, to be viewed as a multilinear map from X^k to R. The $.h^k$ notation means to evaluate $D^k f(x)$ at $(h, \dots, h)$.

If $X = R^2, D^k$ has the following expression $\frac{1}{k!} D^k f(x).h^k = \sum_{|J|=k} \frac{1}{J!} \frac{\partial^{|J|} f}{\partial x^J}(x) h^J$

Where J is a vector of 2 components. The multi-index J runs through all combinations such that $J_1 + J_2 = |J| = k$ in the sum and $J! = J_1! J_2!$

From equation (3), we can rewrite the 2D Taylor expansion as follows:

$$f(x + l, y + k) = f(x, y) + l\frac{\partial f}{\partial x} + k\frac{\partial f}{\partial y} + \frac{1}{2}\left(\frac{\partial^2 f}{\partial x^2}l^2 + 2hl\frac{\partial^2 f}{\partial x \partial y} + \frac{\partial^2 f}{\partial y^2}k^2\right) + O(l^3 + k^3) \qquad (4)$$

From this formula, we take the values of $l = (-1)^n h$ and $k = (-1)^m h$, for $n = \pm 1$ and $m = \pm 1$ to obtain the following 4 formulas :

-For $l = h$ and $k = h$, we obtain:

$$f(x + h, y + h) = f(x, y) + h\frac{\partial f}{\partial x} + h\frac{\partial f}{\partial y} + \frac{h^2}{2}\left(\frac{\partial^2 f}{\partial x^2} + 2\frac{\partial^2 f}{\partial x \partial y} + \frac{\partial^2 f}{\partial y^2}\right) + O(h^3) \qquad (5)$$

- For $l = -h$ and $k = h$, we obtain:

$$f(x - h, y + h) = f(x, y) - h\frac{\partial f}{\partial x} + h\frac{\partial f}{\partial y} + \frac{h^2}{2}\left(\frac{\partial^2 f}{\partial x^2} - 2\frac{\partial^2 f}{\partial x \partial y} + \frac{\partial^2 f}{\partial y^2}\right) + O(h^3) \qquad (6)$$

- For $l = h$ and $k = -h$, we obtain:

$$f(x + h, y - h) = f(x, y) + h\frac{\partial f}{\partial x} - h\frac{\partial f}{\partial y} + \frac{h^2}{2}\left(\frac{\partial^2 f}{\partial x^2} - 2\frac{\partial^2 f}{\partial x \partial y} + \frac{\partial^2 f}{\partial y^2}\right) + O(h^3) \qquad (7)$$

- For $l = -h$ and $k = -h$, we obtain:

$$f(x - h, y - h) = f(x, y) - h\frac{\partial f}{\partial x} - h\frac{\partial f}{\partial y} + \frac{h^2}{2}\left(\frac{\partial^2 f}{\partial x^2} + 2\frac{\partial^2 f}{\partial x \partial y} + \frac{\partial^2 f}{\partial y^2}\right) + O(h^3) \qquad (8)$$

By multiplying the equations (5) and (7) by α and the equation (6) and (8) by β, we obtain the following formula:

$$\alpha f(x + h, y + h) + \alpha f(x + h, y - h) + \beta f(x - h, y + h) + \beta f(x - h, y - h)$$
$$= (2\alpha + 2\beta)f(x, y) + (2\alpha - 2\beta)h\frac{\partial f}{\partial x} + (\alpha + \beta)h^2\Delta f + O(h^3) \qquad (9)$$

Where Δf is the Laplacian of f(x,y).

By replacing h by 2h in (9), we obtain:

$$\alpha f(x + 2h, y + 2h) + \alpha f(x + 2h, y - 2h) + \beta f(x - 2h, y + 2h) + \beta f(x - 2h, y - 2h)$$
$$= (2\alpha + 2\beta)f(x, y) + (4\alpha - 4\beta)h\frac{\partial f}{\partial x} + 4(\alpha + \beta)h^2\Delta f + O(h^3) \qquad (10)$$

Now multiply (9) by γ and add to (10) we deduce that:

$$f(x + 2h, y + 2h) + \alpha f(x + 2h, y - 2h) + \beta f(x - 2h, y + 2h) + \beta f(x - 2h, y - 2h) + \gamma\alpha f(x + h, y + h)$$
$$+ \gamma\alpha f(x + h, y - h) + \gamma\beta f(x - h, y + h) + \gamma\beta f(x - h, y - h)$$
$$= (2\alpha + 2\beta)(\gamma + 1)f(x, y) + (2\alpha - 2\beta)h(\gamma + 2)\frac{\partial f}{\partial x} + (\alpha + \beta)h^2(\gamma + 4)\Delta f + O(h^3)$$

By taking h close to zero, we can neglect h^2 and h^3 and we deduce the following approximation for $\frac{\partial f}{\partial x}$

$$\frac{\partial f}{\partial x} = \frac{1}{(2\alpha - 2\beta)h(\gamma + 2)}\big(\alpha f(x + 2h, y + 2h) + \alpha f(x + 2h, y - 2h) + \beta f(x - 2h, y + 2h)$$
$$+ \beta f(x - 2h, y - 2h) + \gamma\alpha f(x + h, y + h) + \gamma\alpha f(x + h, y - h) + \gamma\beta f(x - h, y + h)$$
$$+ \gamma\beta f(x - h, y - h) - (2\alpha + 2\beta)(\gamma + 1)f(x, y)\big) \tag{11}$$

Note that the approximation (11) is of order 1, if $\gamma = -4$, the term $(\alpha + \beta)h^2(\gamma + 4)\Delta f$ disappears and the approximation is of order 2.

By multiplying the equations (5) and (6) by α and the equation (7) and (8) by β, we can obtain the following formula:

$$\alpha f(x + h, y + h) + \alpha f(x - h, y + h) + \beta f(x + h, y - h) + \beta f(x - h, y - h)$$
$$= (2\alpha + 2\beta)f(x, y) + (2\alpha - 2\beta)h\frac{\partial f}{\partial y} + (\alpha + \beta)h^2\Delta f + O(h^3) \tag{12}$$

Replace h by 2h in (12) to obtain

$$\alpha f(x + 2h, y + 2h) + \alpha f(x - 2h, y + 2h) + \beta f(x + 2h, y - 2h) + \beta f(x - 2h, y - 2h)$$
$$= (2\alpha + 2\beta)f(x, y) + (4\alpha - 4\beta)h\frac{\partial f}{\partial y} + 4(\alpha + \beta)h^2\Delta f + O(h^3) \tag{13}$$

In Paper [6], the order of the approximation is 1, to increase the order of the approximation we introduce a new parameter γ. We will show that for a special value of γ the order of the approximation is 2. Now multiply (12) by γ and add to (10) we deduce :

$$\alpha f(x + 2h, y + 2h) + \alpha f(x - 2h, y + 2h) + \beta f(x + 2h, y - 2h) + \beta f(x - 2h, y - 2h) + \gamma\alpha f(x + h, y + h)$$
$$+ \gamma\alpha f(x - h, y + h) + \gamma\beta f(x + h, y - h) + \gamma\beta f(x - h, y - h)$$
$$= (2\alpha + 2\beta)(\gamma + 1)f(x, y) + (2\alpha - 2\beta)h(\gamma + 2)\frac{\partial f}{\partial y} + (\alpha + \beta)h^2(\gamma + 4)\Delta f + O(h^3)$$

Similarly, we can deduce the following approximation for $\frac{\partial f}{\partial y}$

$$\frac{\partial f}{\partial y} = \frac{1}{(2\alpha - 2\beta)h(\gamma + 2)}\big(\alpha f(x + 2h, y + 2h) + \alpha f(x - 2h, y + 2h) + \beta f(x + 2h, y - 2h)$$
$$+ \beta f(x - 2h, y - 2h) + \gamma\alpha f(x + h, y + h) + \gamma\alpha f(x - h, y + h) + \gamma\beta f(x + h, y - h)$$
$$+ \gamma\beta f(x - h, y - h) - (2\alpha + 2\beta)(\gamma + 1)f(x, y)\big) \tag{14}$$

Note that the approximation (14) is of order 1, if $\gamma = -4$, the term $(\alpha + \beta)h^2(\gamma + 4)\Delta f$ disappears and the approximation is of order 2.

From the above formulas (11) and (14), we construct the 5x5 horizontal masks as follows:

$$M_x = \frac{1}{(2\alpha - 2\beta)h(\gamma + 2)}\begin{pmatrix} \beta & 0 & 0 & 0 & \beta \\ 0 & \gamma\,\beta & 0 & \gamma\beta & 0 \\ 0 & 0 & (2\beta + 2\alpha)(\gamma + 1) & 0 & 0 \\ 0 & \gamma\,\alpha & 0 & \gamma\,\alpha & 0 \\ \alpha & 0 & 0 & 0 & \alpha \end{pmatrix}$$

The Sobel 5x5 horizontal and vertical mask are [1]

Similarly, we can write the My Mask as following:

$$My = \frac{1}{(2\alpha - 2\beta)h(\gamma + 2)} \begin{pmatrix} \alpha & 0 & 0 & 0 & \beta \\ 0 & \gamma\,\alpha & 0 & \gamma\beta & 0 \\ 0 & 0 & (2\beta + 2\alpha)(\gamma + 1) & 0 & 0 \\ 0 & \gamma\,\alpha & 0 & \gamma\beta & 0 \\ \alpha & 0 & 0 & 0 & \beta \end{pmatrix}$$

The Sobel 5x5 horizontal and vertical mask are   [1]

$$Mx = \begin{pmatrix} -1 & -4 & -6 & -4 & -1 \\ -2 & -8 & -12 & -8 & -2 \\ 0 & 0 & 0 & 0 & 0 \\ 2 & 8 & 12 & 8 & 2 \\ 1 & 4 & 6 & 4 & 1 \end{pmatrix} \text{ and } My = \begin{pmatrix} 1 & 2 & 0 & -2 & -1 \\ 4 & 8 & 0 & -8 & -4 \\ 6 & 12 & 0 & -12 & -6 \\ 4 & 8 & 0 & -8 & -4 \\ 1 & 2 & 0 & -2 & -1 \end{pmatrix}$$

[4] Experimental Results

In this section, we applied our proposed operator on three lung CT-Scan images and we choose α=1, β=-2 and γ=1.

- Image figure 1a presents the original CT-Scan lung image. Image in figure 1b presents the result of new operator in x-direction. Image in figure 1c presents the result of new operator in y-direction. Image in figure 1d presents the result of Sobel operator in x-direction. Image in figure 1e presents the result of Sobel operator in y-direction. Note that in this image, our proposed operator gave better results than Sobel operator.
- Image figure 2a presents the original CT-Scan lung image. Image in figure 2b presents the result of new operator in x-direction. Image in figure 2c presents the result of new operator in y-direction. Image in figure 2d presents the result of Sobel operator in x-direction. Image in figure 2e presents the result of Sobel operator in y-direction. Note that in this image, our proposed operator gave better results than Sobel operator.
- Image figure 3a presents the original CT-Scan lung image. Image in figure 3b presents the result of new operator in x-direction. Image in figure 3c presents the result of new operator in y-direction. Image in figure 3d presents the result of Sobel operator in x-direction. Image in figure 3e presents the result of Sobel operator in y-direction. Note that in this image, our proposed operator gave better results than Sobel operator.

(a): Original CT-Lung image
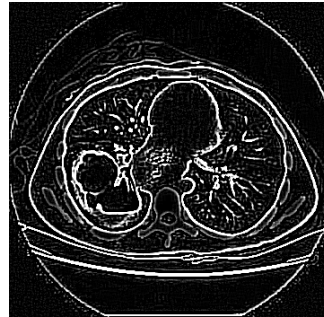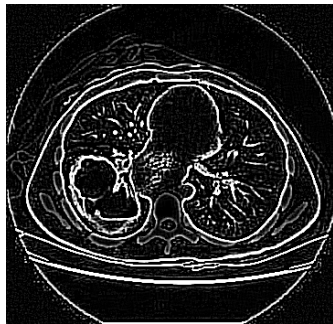
(b): Result of the proposed 5x5 mask in x-direction

Result of the proposed 5x5 mask in y-direction

(d) Sobel 5x5 Mask in x-direction

(e) : Sobel 5x5 Mask in y-direction

Figure 1. Results of our proposed method and 5x5 Sobel masks
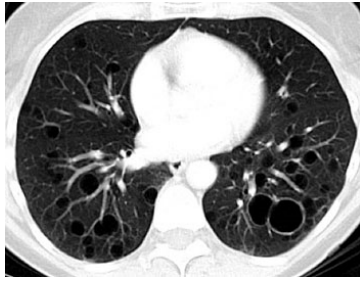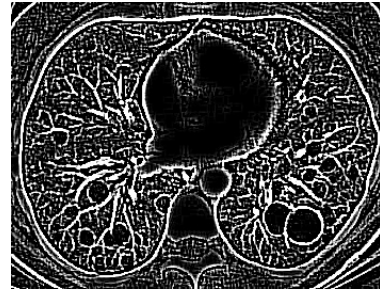
(a): Original CT-Lung image

(b): Result of the proposed 5x5 mask in x-direction
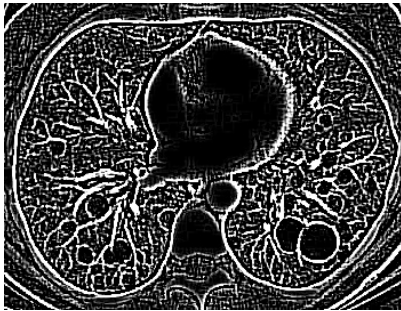
Result of the proposed 5x5 mask in y-direction

(d Sobel 5x5 Mask in x-direction

(e) : Sobel 5x5 Mask in y-direction

Figure 2. Results of our proposed method and 5x5 Sobel masks
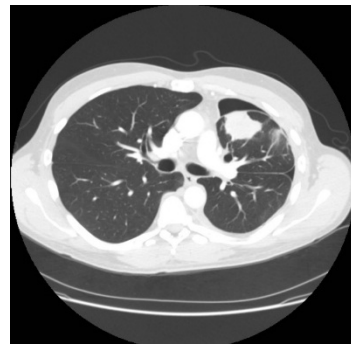
(a): Original CT-Lung image
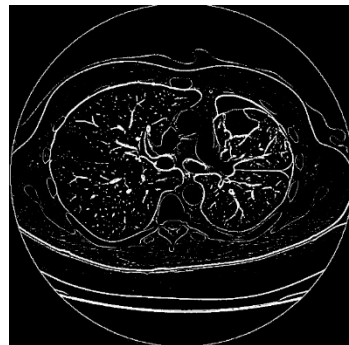
(b): Result of the proposed 5x5 mask in x-direction
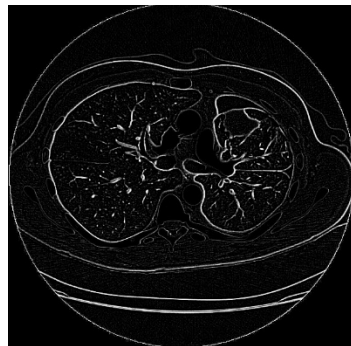
(c)Result of the proposed 5x5 mask in y-direction
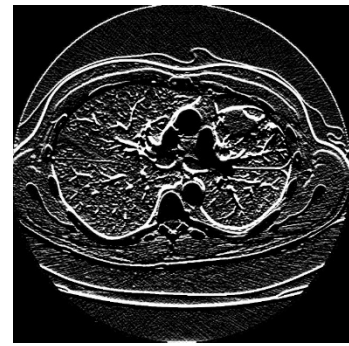
(d) Sobel 5x5 Mask in x-direction
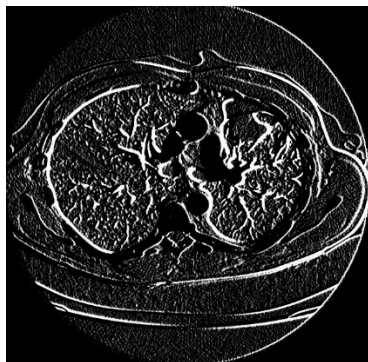
(e) Sobel 5x5 Mask in y-direction

Figure 3. Results of our proposed method and 5x5 Sobel masks

[5] **Conclusion and Future Works**

In this paper, we presented a new method for detecting edges in CT-Scan lung images. The proposed method is based on the finite difference method. In previous operator [15], the masks are constructor using 2 parameters but in this paper we added a third parameter in order to have more general masks. The new masks are applied three CT-Scan images and we obtained good results in comparison with Sobel

5x5 masks. The objective of the proposed method is to detect edges in lung images, as future work, we have to develop another method in order to reconstruct the entire boundaries of lung in order to define well the candidate cancer region.

REFERENCES

[1]   Gonzalez R. and Woods R., "Digital image processing," 3rd Edition, Prentice Hall, New York, 2008, pp. 695.

[2]   Edge Detection and Segmentation of Multiple Contours from CT Scan Images Amba D. Bhatt , Ujjaval Gupta , Vishal Wagholikar , Uday V. Pise Computer-Aided Design and Applications Vol. 9, Iss. 4, 2012

[3]   COMPARATIVE ANALYSIS OF VARIOUS IMAGE EDGE DETECTION TECHNIQUES FOR TWO DIMENSIONAL CT SCAN NECK DISC IMAGE, J Preetha, S Selvarajan and P Suresh, International Journal of Computer Science & Communication, Vol. 3, No. 1, January-June 2012, pp. 57-61.

[4]   EDGE DETECTION FROM CT IMAGES OF LUNG , S. K. BANDYOPADHYAY, INTERNATIONAL JOURNAL OF ENGINEERING SCIENCE & ADVANCED TECHNOLOGY, Volume - 2, Issue - 1, 34 – 37.

[5]   A Novel Approach of Cancerous Cells Detection from Lungs CT Scan Images , N. Pandey ,S. Nandy International Journal of Advanced Research in Computer Science and Software Engineering , Volume 2, Issue 8, August 2012.

[6]   T. El-Arwadi and A. El-Zaart, A Novel 5x5 Edge Detection Operator For Blood Vessel Images, accepted at the British Journal of Applied Science & Technology, accepted August 2015.

[7]   Wafaa Kamel Al-Jibory and Ali El-Zaart "A New Edge Detector in CT Scan Images Using Gradient of Weibull Distribution", World of Computer Science and Information Technology Journal (WCSIT), Vol. 4, No. 1, 13-17, 2014.

[8]   Canny J. "A Computational Approach to Edge Detection Edge Detection". IEEE Transactions on Pattern Analysis and machine intelligence, Vol. PAMI-8, NO. 6, November 1986.

Online Spatial Cancer Registry System for Nigeria

Adebayo Peter Idowu[1], Kehinde Oladipo Williams[2], Bunmi Alonge[1] and Olusegun Ajibola Sarumi[1]
[1]Department of Computer Science & Engineering, Obafemi Awolowo University, Ile-Ife, Nigeria
[2]Department of Physical and Computer Sciences, College of Natural and Applied Sciences, McPherson University, Ajebo, Ogun State, Nigeria
kehindewilliams@yahoo.com; paidowu1@yahoo.com

ABSTRACT

Cancer has become a major source of morbidity and mortality globally. The incidence of cancer is rising as well as in Nigeria as it continues to eat deep into the nation claiming lives of both prominent and less prominent citizens of the country. This disease is increasingly taking the lives of productive citizens thereby adding to the poverty level of the nation. In this paper, we present a system which was developed for population based cancer registry in Nigeria. This system is an online system with spatial features.

 The online spatial cancer registry for Nigeria was developed using Adobe Dreamweaver and Notepad++ as the Integrated Development Environments, HTML, CSS and JavaScript were used for the frontend, PHP was used as the scripting language, and MySQL with google map. The software used were open source which ensured that the application would be robust, reusable, cheap and highly scalable.

The result of the developed system shows that health officers, policy makers and all other authorized stakeholders would be able to register, login, and run queries on information that has been previously entered into the system. With the system, the spatial distribution of cancer in any location in Nigeria can be easily visualized and query. Policy makers and authorized users would be able to visualize and query the system in order to take appropriate steps in addressing cancer in Nigeria.

In conclusion, this system will help create national database for cancer patients and be able to analyse the spatial distribution of cancer and the system is user-friendly.

Keywords: Cancer, Registry, Spatial, Online, Open Source

[6] Introduction

Cancer is a group of diseases characterized by unregulated division and spread of cells. The cancerous cells may occur in liquids, as in leukaemia (American Cancer Society, 2008). Most cancer, however, occur in solid tumours that originally appear in various tissues in various parts of the body. By their original locations they are classified into various types of cancer, such as lung, colon, breast, prostate cancer, etc. Localized tumours can be removed by surgery or irradiation with high survival rates. As cancer progresses, however, it metastasizes – invading the surrounding tissues, entering the blood stream, spreading and establishing colonies in distant parts of the body (American Cancer Society, 2008). Only a third of patients with metastasized cancer survive more than five years. Invasive distensions spreading crab-like from a

tumour in the breast were described by Hippocrates. From the crab, karkinos in Greek and cancer in Latin, came the name of the disease and the name of its inducing agents, carcinogens (Dervan, 1999).

In 2007, there were 11 million cancer cases, 7 million cancer deaths and 25 million people living with cancer. This is projected to increase to 27 million cases, 17 million deaths and 75million people living with cancer in 2050 (World Health Organisation, 2006). Cancer is a leading cause of disease worldwide. An estimated 14.1 million new cancer cases occurred in 2012. Lung, female breast, colorectal and stomach cancers accounted for more than 40% of all cases diagnosed worldwide. In men, lung cancer was the most common cancer (16.7% of all new cases in men). Breast cancer was by far the most common cancer diagnosed in women (25.2% of all new cases in women) (World Cancer Factsheet, 2014). Cancer is a leading cause of death worldwide, with 8.2 million deaths in 2012. More than half of all cancer deaths each year are due to lung, stomach, liver, colorectal and female breast cancers (World Cancer Factsheet, 2014).

Cancer is a major public health burden in both developed and developing countries. It is the second largest common disease spread world-wide (Kainsa et al., 2012). When a cell is damaged or altered without repair to its system, it usually dies. But if such damaged or unrepaired cells do not die and proliferate with uncontrolled growth; a mass of cancer cells develop. Cancer has a complex aetiology with multiple risk factors that involve the interplay between genetic and environmental influences. The redox dysregulation originates from metabolic alterations and it is dependent on mitogenic and survival signalling through reactive oxygen species. There is a delicate balance between the production and the destruction of reactive species; for this, we need to understand the role of redox homeostasis in cancer. So, the specific vulnerability of the malignant cells can be selectively targeted (Dawane and Pandit, 2012).

A cancer registry is an information system designed for the collection, management and analysis of data on persons with the diagnosis of a malignant or neoplastic disease (National Cancer Registry Association, 2014). Hospital-based cancer registries which are also referred to as Health care institution registries are concerned with the recording of information on the cancer patients seen in a particular hospital, maintain data on all patients diagnosed and/or treated for cancer at their facility. Population-based cancer registries also known as Central Registries seek to collect data on all new cases of cancer occurring in a well defined population, maintain data on all cancer patients within certain geographical areas. Special purpose registries maintain data on a particular type of cancer, such as brain tumours. Maintaining a Cancer Registry ensures that health officials have accurate and timely information, while ensuring the availability of data for treatment, research, and educational purposes.

The aim of this paper is to develop an online cancer registry for Nigeria with spatial feature. This spatially captures cases of cancer in the hospitals and stores information about the cases of cancer and type of cancer in any location in Nigeria. This system can be used by health officers and policy makers to know the distribution of each type of cancer in any location in Nigeria and this will allow them to take appropriate policy that will handle the health challenge. It will also make them to know type of cancer peculiar to each location and aid in querying why such cancer is paramount in the location.

[7] **Cancer in Nigeria**

The burden of cancer in Nigeria is unknown; mainly because of lack of statistics or under-reporting. This is not peculiar to only Nigeria but most parts of Africa. In a study of cancer registry literature update from all over the world, only 1% of the literature emanated from Africa compared to 34% and 42% from Europe

and Asia respectively. This is partly due to inaccurate population statistics which makes age specific incidence rates impossible or if available inaccurate (World Health organisation, 2008).

Annually, there are about 100,000 new cancer cases in Nigeria, this is estimated to increase to 500,000 in 2010. It was estimated that incidence of cancer in Nigerian men and women by 2020 will be 90.7/100,000 and 100.9/100,000 and the deaths rates will be 72.7/100,000 and 76,000/100,000, respectively (World Health organisation, 2008).

Cancer currently accounts for 4.4% of all deaths and is likely to increase to 6.8% in 2030 (World Health organisation, 2008). Out of 89,000 cancer deaths in 2005; 54,000 of these were younger than 70 years. The commonest cancers of Nigerian men are cancers of prostate, liver and lymphomas (Parkin, 2003; Awodele et al., 2011). In the women, cancer of cervix and breasts are commonest with minimal regional variation.

The Ibadan cancer registry showed a reduction in age standardized mortality rate from 1960 to 1999. This was attributed to introduction of user fees and reduction in the coverage area. While cervical cancer is commonest in Zaria, Northern Nigeria (Abioye, 198) as in rest of Africa (Ngoma, 2006), breast cancer has become the commonest cancer of women in Ibadan, Southern Nigeria (Awodele et al., 2011; Parkin, 2003). These common cancers should be the focus of cancer control programs in Nigeria.

Moreover, due to the epidemiological shift, increase in ageing population, high rate of infections and entrenchment of the modifiable risk factors, cancers will yet pose significant challenge to Nigeria and other developing countries which currently lack cancer control programs directed at reducing cancer incidence and mortality and to improve quality of life. There are very few human and material resources for cancer control in developing countries where cancers occur at younger ages, 70% of cancer deaths occur and only 5% of global funds for cancer control is present (World Health Organisation, 2002).

Large proportions of the population still never seek orthodox medical care and so are not recorded. Other reasons are inadequate diagnostic facilities, limited access to care, inadequate technical manpower and infrastructure as well as quality of cancer data systems all contribute to inaccurate data on cancer burden.

[8] **Related Literature**

Cancer is a public health problem worldwide affecting all categories of persons. Cancer is a major public health burden in both developed and developing countries. It is the second largest common disease spread world-wide (Kainsa et al., 2012). It is the second common cause of death in developed countries and among the three leading causes of death in developing countries (World Health Organisation, 2005).

Cancer is a leading cause of disease worldwide. It is the second most common cause of death; constituting 12% of all deaths after cardiovascular disease. It kills more people than Tuberculosis, HIV/AIDS and Malaria combined (World Health Organisation, 2006). In 2007, there were 11 million cancer cases, 7 million cancer deaths and 25 million people living with cancer. This is projected to increase to 27 million cases, 17 million deaths and 75million people living with cancer in 2050 (World Health Organisation, 2008).

An estimated 14.1 million new cancer cases occurred in 2012. Lung, female breast, colorectal and stomach cancers accounted for more than 40% of all cases diagnosed worldwide. In men, lung cancer was the most common cancer (16.7% of all new cases in men). Breast cancer was by far the most common cancer

diagnosed in women (25.2% of all new cases in women) (World cancer factsheet, 2014). Cancer is a leading cause of death worldwide, with 8.2 million deaths in 2012. More than half of all cancer deaths each year are due to lung, stomach, liver, colorectal and female breast cancers (World Cancer Factsheet, 2014). Approximately 44% of cancer cases and 53% of cancer deaths occur in countries at a low or medium level of the Human Development Index (HDI) (World Cancer Factsheet, 2014).

Liver cancer in men is the fifth most frequently diagnosed cancer worldwide but the second most frequent cause of cancer death. In women, it is the seventh most commonly diagnosed cancer and the sixth leading cause of cancer death. An estimated 748,300 new liver cancer cases and 695,900 cancer deaths occurred worldwide in 2008. Half of these cases and deaths were estimated to occur in China. Globally, rates are more than twice as high in males as in females. The highest liver cancer rates are found in East and South-East Asia and in Middle and Western Africa, whereas rates are low in South-Central and Western Asia, as well as Northern and Eastern Europe (World Cancer Factsheet, 2014).

If recent trends in major cancers are seen globally in the future, the burden of cancer will increase to 23.6 million new cases each year by 2030. This represents an increase of 68% compared with 2012 (66% in low and medium HDI countries and 56% in high and very high HDI countries) (World cancer factsheet, 2014).

Cancer is an emerging public health problem in Africa. According to the International Agency for Research on Cancer (IARC), about 681,000 new cancer cases and 512,400 cancer deaths occurred in 2008 in Africa. These numbers are projected to nearly double (1.28 million new cancer cases and 970,000 cancer deaths) by 2030 simply due to the aging and growth of the population, with the potential to be even higher because of the adoption of behaviours associated with western lifestyles, such as smoking, unhealthy diet, and physical inactivity (International Agency for Research on Cancer, 2014). Despite this growing burden, cancer continues to receive low public health priority in Africa, largely because of limited resources and other pressing public health problems, including communicable diseases such as acquired immune deficiency syndrome (AIDS)/human immunodeficiency virus (HIV) infection, malaria, and tuberculosis. It may also be in part due to a lack of awareness about the magnitude of the current and future cancer burden among policy-makers, the general public, and international private or public health agencies interested in global health.

Cancers related to infectious agents (cervix, liver, Kaposi sarcoma, urinary bladder) are among the dominant forms of cancer in Africa. In 2008, cervical cancer accounted for 21% of the total newly diagnosed cancers in females and liver cancer for 11% of the total cancer cases in males (International Agency for Research on Cancer, 2014; America Cancer Society, 2014). Parkin et al (2008) reported that in indigenous Africans, 650,000 people of estimated 965million are diagnosed of cancer annually and lifetime risk of dying from cancer in African women is 2 times higher than in developed countries.

Africa carries an increasing cancer burden, 75% of the 650,000 annual cases present late, at younger ages and about 510,000 deaths occur (Ngoma, 2006). The incidence ranges from 70/100,000 to- 100/100,000 people. Infectious agents like Hepatitis B, C, Human Papilloma Virus (HPV), Helicobacter pylori contribute significantly to cancers in developing countries. The HIV pandemic is changing the pattern and prevalence of cancer especially in East Africa where AIDS-related cancers like Kaposi sarcoma, lymphomas, anal cancers and cervical cancers are increasing (Parkin, 2003). Kaposi sarcoma (15.5%) is now the commonest cancer of men in sub-Saharan Africa and cervical cancer (22.2%) is commonest in women (Ngoma, 2006).

The World Health Organisation has developed guidelines for regional and national cancer control programs according to national economic development. In its 58th World Health Assembly in 2005, the World Health Organisation urged member states to develop and reinforce comprehensive and evidence-based cancer control programs in order to curb the growing global burden of cancer.

It might seem that cancer registration should not be regarded as a priority for the health services of a developing country, given all the competing demands upon the limited resources allocated to health. However, cancer is already a significant health problem in many developing countries. More than half of the new cancer cases in the world occur in developing countries (Parkin et al., 1993). The rapid increase in life expectancy (largely because of a reduction in mortality from infectious disease) together with the adoption of western lifestyles suggests that the burden of cancer in these countries is likely to increase in the near future.

Most often cancer registries provide the only opportunity of properly assessing the extent and nature of the cancer burden in developing countries, since very few of them have reliable cause-specific mortality data. Ideally, the objective should be to establish a population-based cancer registry which will be able to estimate the incidence of different tumours in a well-defined community. However, because of the relative ease with which they can be established, cancer registries in developing countries often start on the basis of cases attending certain hospitals or departments of histopathology. Population-based cancer registries in developing countries usually face enormous logistic problems due to lack of appropriately trained personnel and adequate resources. In addition, their success may be jeopardized by external factors beyond their control.

[9] **Methodology**

The system was developed using web-based technologies like HTML5 and Cascading Styling Sheets (CSS3) for the styles of the pages designed, these were used for the front end design of the cancer registry. The geographical distribution of cancer was made available using the Google Map Maker. Finally, the prototype system was developed using WAMP (Web-Apache-MySQL-PHP) server software through local-hosting services. The spatial features introduced through Google Map was incorporated into the system using PHP and HTML.

WampServer was used to write MySQL queries for populating the database. The prototype was implemented using Adobe Dreamweaver; Apache was used as the web server to provide the basic functionality of the monitoring system. PHP was used as a scripting language to program the server-side manipulation of the knowledge in the database.

[10]**Prototype Implementation**

The user interface allows the user to navigate the system and also facilitate interact with the database. The system is simple and user friendly through the use of Windows Interface Menu (WIMP), and pointing devices which is very important in computer graphics design and architecture. Hence, the online spatial cancer registry for Nigeria was designed to accommodate health officers and policy officers with varying skills. A well designed and simple user interface provides user with a better understanding of the system.

a. The home page module

The home page is the first interface that the user views the moment the universal resource locator (URL) of the cancer registry is accessed (see figure 1). The home page is where the user can be able to access the buttons to navigate to every other part of the registry. For all registered users who want to perform any activity on the system, the user must click on the menu button (login) in order to log in and perform any necessary functions required.
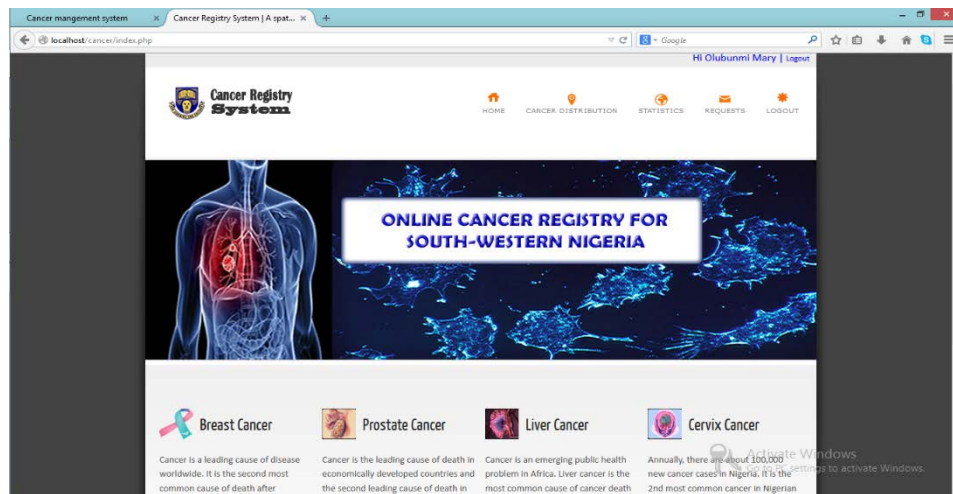
Figure 1: Home Page Module

b. The user registration module

User registration module is the module which allows all the users to send registration request to the admin (in this case the Registrar) by entering their personal details and necessary identifications indicating the type or category of user they belong to. In this module, each user is required to enter their name(s), username, password, e-mail address, agency/hospital name, user type, identification type, identification image and passport. The user then waits for his or her request to be approved by the registrar of the cancer registry. Figure 2 depicts the user registration module.
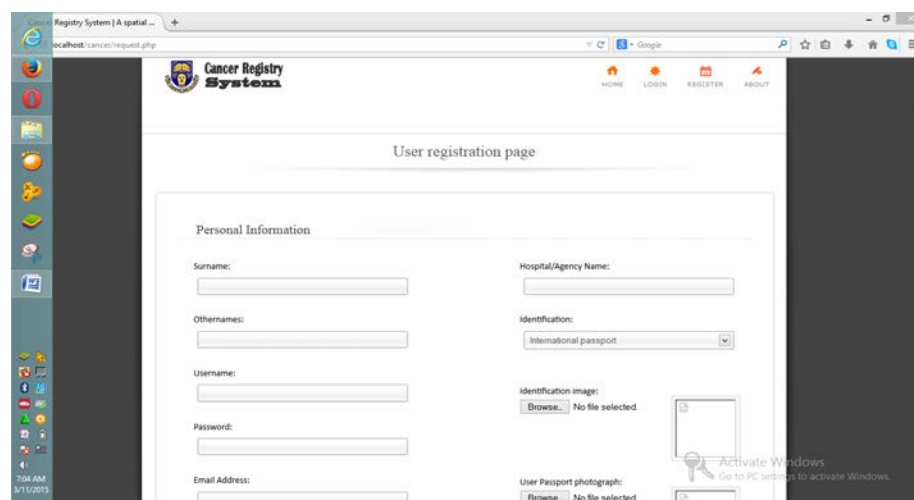
Figure 2: User Registration Module

c. The login module

This module is the module that enables the approved users of the cancer registry to log in to the registry to perform all authorised activities within the jurisdiction of their user type. This module has the username, password and user type boxes. It also has a provision for the users that are yet to be registered to do so. The login module is depicted in figure 3.
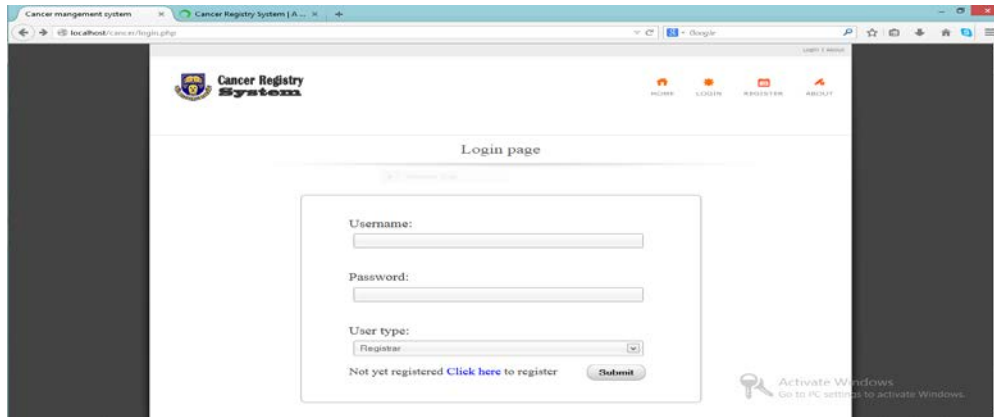
Figure 3: Login Module

d. The cancer distribution module

The cancer distribution module is simply the geographical display of the spread of cancer in a map of the area of study. It displays the various towns in south-western Nigeria that have any record of persons living with cancer and the types of cancer registered in the database of the cancer registry. The cancer distribution module can only be functional or available as long as there is internet connection on the device being used to access the cancer registry. All authorised users of the cancer registry can access this module. See figure 4 for the cancer distribution module.
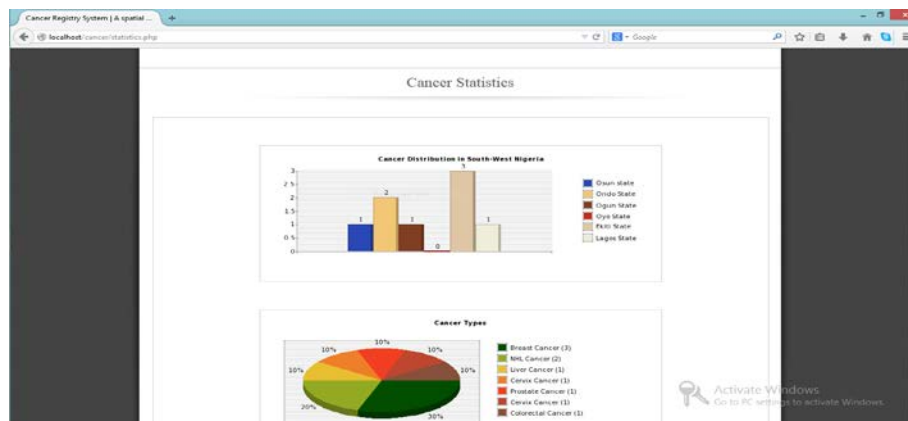
Figure 4: Cancer Distribution Module

e. The registration requests module

This module is the module that is accessed only by the registrar or any other authorised personnel of the cancer registry; this module enables the approval of the request sent in by anyone registering to become a user of the system. The registration requests module consist the user ID, names of the users, the

username, the user type, the hospital or organization name, the date of registration, the registration status of the user, action performed by the registrar. See figure 4 for the registration requests module.

Figure 5: Registration Request Module

f. The cancer distribution module

The cancer distribution module is simply the geographical display of the spread of cancer in a map of the area of study. The map as shown in figure 4 displays the various towns in south-western states of Nigeria that have any record of persons living with cancer and the types of cancer registered in the database of the cancer registry. The cancer distribution module can only be functional or available as long as there is internet connection on the device being used to access the cancer registry. All authorised users of the cancer registry can access this module.
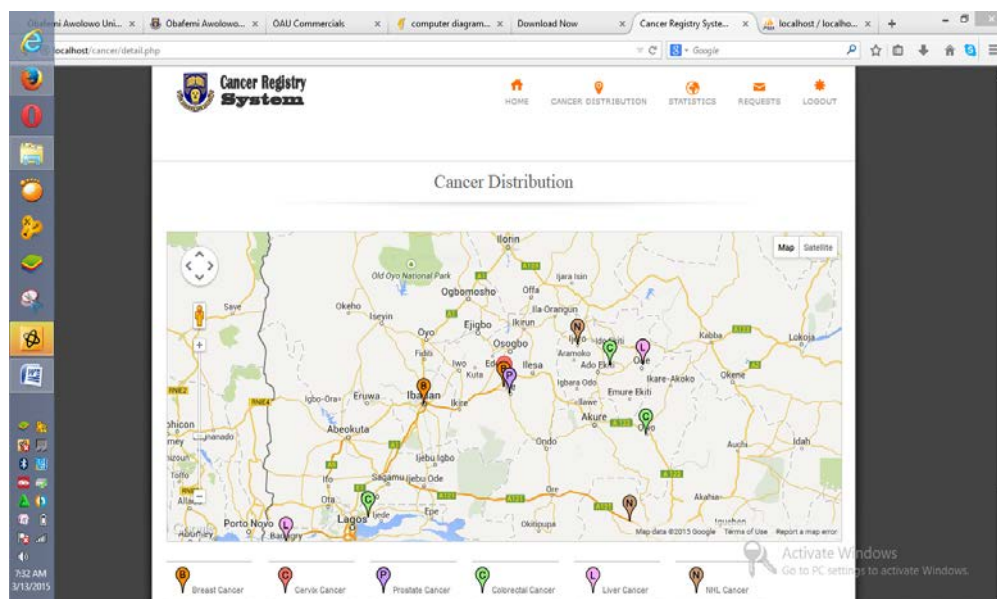
Figure 6 Cancer Distribution Module

g. Discussion

The cancer registry information system was developed using the adopted data model to gather information comprehensively about cancer patients which will help monitor and control the widespread of the disease and provide a database for south-western Nigeria for monitoring and controlling of cancer and tumours generally. This will also help in determining the distribution rate of cancer in south-western Nigeria and the prevalence rate of cancer in this region of the country. The proposed system allows for the users to register information, view cancer statistics and cancer distribution in different towns of south-west in Nigeria based on their user type.

The project work makes use of bar charts, pie chart and map in order to allow for easy to understand and easy-to-interpret information view. Users can view cancer distribution details of any location on the map within the area of study with ease. This will help policy makers in making decisions regarding building cancer related health facilities and distribution of can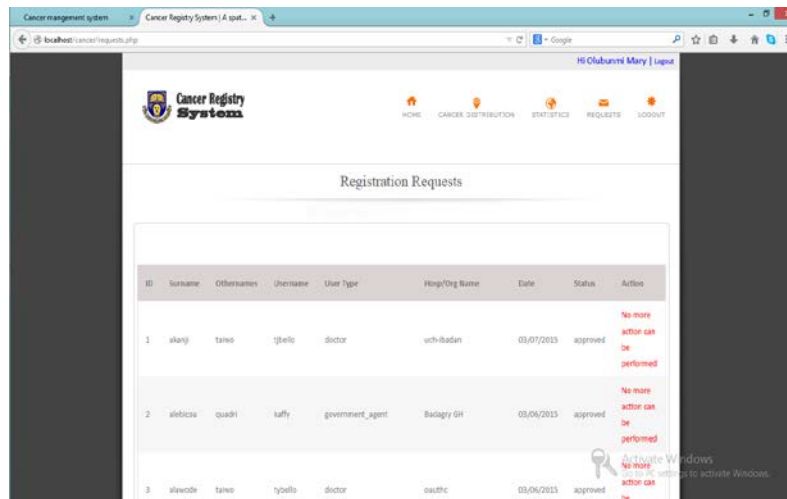cer equipment. The model in future may give arise to a comprehensive cancer registry for Nigeria as a whole. Also, oncologists, policy makers, and any other authorised users would be able to query, analyse, view and generate cancer distribution information based on cancer types, town/city and state level and this will enhance proper and wide cancer prevention awareness campaign.

This system will hopefully aid effective and efficient intervention in the rate at which cancer is claiming lives of Nigerians. This will improve the standard of health care system especially those related to cancer and tumours generally. This system will also serve as a way of having uninterrupted access to genuine information on cancer distribution (either hard copy or on the internet) in the nation.

[11]Conclusion

This paper focuses on GIS based cancer population registry for Nigeria; it will indeed serve as reliable information storage and retrieval system of cancer incidence in Nigeria. The system testing showed the effectiveness and user-friendliness of the system in terms of information storage and retrieval time, the cancer distribution display on the map and the graphical user interface design. The system was designed and developed to capture cancer patient's information such as the name, gender, occupation, marital status, ethnicity, cancer type, cancer level, nationality, residential address, state of origin etc.

The system can display the cancer distribution of the various types of cancer in various locations on the map in terms of residential address of the patients. It is also able to display the cancer statistic in terms of gender, state, ethnicity and cancer types. The system will go a very long way in helping government and non-governmental agencies (NGOs) in providing necessary, proper and adequate cancer health care facilities in the nation that help improve the life of people living with cancer as well as prevent the death of citizens through early diagnosing and treatment. It will also enhance the channelling of campaigns on how to combat cancer to the right areas in the nation.

REFERENCES

[1]   Abioye AA(1981), The Ibadan Cancer Registry. 1960-1980: Cancer in Africa proceedings of a workshop of the West African College of Physicians: Monrovia, Liberia: 6th-9th July, 1981.

[2]   American Cancer Society (2008). Cervical Cancer. Available from www.cancer.org [Accessed July 17, 2014]

[3]   Ananya   Mandal,   MD   (2012)   Cancer   Symptoms   News-Medical.   Available   from http://www.news-medical.net/health/Cancer-Symptoms.aspx [Accessed December 2, 2014]

[4]   Ananya Mandal, MD (2012) Cancer Classification. News-Medical Available from
        http://www.news-medical.net/health/Cancer-Classification.aspx [Accessed December 2, 2014]

[5]   Awodele, O., Adeyomoye, A.A., Awodele, D.F., Fayankinnu, V.B., and Dolapo, D.C. (2011). Cancer distribution pattern in southwestern Nigeria. Tanzania Journal of Health Res., 13(2), 106-108.

[6]   CancerCare (2014). Lung Cancer 101. Available from www.lungcancer.org [Accessed March 7, 2015]

[7]   Peter A. Dervan (1999). Understanding Cancer: A Scientific and Clinical Guide for the Layperson. ISBN 0-7864-0628-3 McFarlansd & Company, Inc., Publisher

[8]   Dewane JS, and Pandit VA.(2012). Understanding Redox Homeostasis and its Role in Cancer. Journal of Clinical and Diagnostic Research, 6(10):1796-1802.

[9]   GLOBOCAN (2012). Estimated Cancer Incidence, Mortality and Prevalence Worldwide in 2112. Available from http://globocan.iarc.fr/Default.aspx [Accessed March 14, 2015]

[10]   International Agency for Research on Cancer (2014). Making the population-based cancer registry. Planning and Developing Population Based Cancer registration in Low and Middle-Income   Settings,   IARC   Technical   Publications   Available   from http://www.iarc.fr/en/publications/pdfs-online/treport-pub/treport-pub43/ [Accessed March 7, 2015]

[11]   Kainsa et al (2012). Medicinal Plants of Asian Origin having Anticancer Potential: Short Review. Asian Journal of Biomedical and Pharmaceutical Sciences. 2(10)

[12]   Moore, D. A., and Carpenter, T. E. (1999). Spatial Analytical Methods and Geographic Information Systems: Use in Health Research and Epidemiology. Epidemiologic Review, 21(2), 143-161

[13]   National Cancer Institute (2003). Cancer and the Environment: What you   need to know, what   you   can   do.   Available   from http://www.niehs.nih.gov/health/materials/cancer_and_the_environment_508.pdf [Accessed March 12, 2015]

[14]   National Cancer Institute (2008). National Cancer Institute, Where can I find Cancer Incidence Statistics?   Available   from   http://surveillance.cancer.gov/statistics/types/incidence.html [Accessed March 12, 2015]

[15]   National   Cancer   Institute   (2014).   Stomach   Cancer.   Available   from http://www.cancer.gov/researchandfunding/snapshots/stomach [Accessed January 12, 2015]

[16]   National Cancer Registry Association (2014). The Cancer Registry and   the Registrar. Available from http://www.ncra-usa.org/i4a/pages/index.cfm?pageid=3862 [Accessed January 25, 2015]

[17]   Ngoma, T. (2006). World Health Organisation. Cancer Priorities in Developing Countries. Annals of Oncology, 17: 9 –14.

[18]   Parkin D.M (2013). Cancer Registration in Emerging Health Systems: The   INCTR   Cancer Registry   Programme   Available   from   http://cancercontrol.info/wp-content/uploads/2014/08/cc2013_55-59-Maxwell-Parkin-incl-T-page_2013.pdf   [Accessed February 16, 2015]

[19]   Parkin D.M (2008). The role of Cancer registries in cancer control. Int. Journal of Clinical Oncol.; 13(2): 102-105

[20]   Parkin D. M., Bray F. I., Devesa S. S. (2003) Cancer Burden in the year 2000-The global picture. European Journal of Cancer, S4-S66

[21]   World   Cancer   Factsheet   (2014).   World   Cancer   Burden.   Available   from http://publications.cancerresearchuk.org/downloads/product/CS_REPORT_WORLD.pdf [Accessed March 18, 2015]

[22]   World Health Organization (2006). Cancer control: knowledge into action: WHO guide for effective programmes. Geneva, Switzerland.

[23]   World Health Organization (2008). World Health Statistics. WHO, Geneva.

[24]   World Health Organization (2009). Cancer. Available from http://www.who.int/mediacentre/factsheets/fs297/en/index.html [Acessed December 21, 2014]

Automatic Segmentation of Multiple Sclerosis Lesions in Brain MR Images

[1]Mohaddeseh Peyvandi and [2]Ali A. Pouyan
School of Computer Engineering, Shahrood University of Technology, Shahrood, Iran;
[1]peyvandisogand@gmail.com; [2]apouyan@shahroodut.ac.ir

ABSTRACT

Magnetic resonance (MR) imaging is one of the most important tools for multiple sclerosis (MS) diagnosis. However, detection and segmentation of MS lesion in MR images is challenging. Variability in lesion location, size, shape, and anatomical variability between subjects are some factors that cause accurate identification of MS lesions in MR images extremely difficult. On the other hand, manual segmentation is time-consuming. Furthermore, it is subject to observer variability. Several methods have been proposed to automatically segment MS lesions. They have been classified as supervised and unsupervised approaches. In this paper, we used both strategies, using combination of hidden Markov random field (HMRF), k-nearest neighbors (KNN) and support vector machine (SVM) algorithms. The performance of proposed approach is quantitatively evaluated on 20 MS patients that have provided by MS lesion segmentation grand challenge dataset (MICCAI 2008). The average value of dice coefficient percentage (80.03%) and Positive Predictive Value (0.7661) are computed by spatially comparing the results of present procedure with expert manual segmentation. The results showed acceptable performance for the proposed approach, compared to those of previous work.

Keywords: Multiple Sclerosis; MS lesion; MR image; Brain segmentation.

[12]Introduction

Multiple sclerosis (MS) is known as a chronic inflammatory disease of the central nervous system (CNS) [1]. In people with MS, immune system damage to the isolating layer of myelin around the nerve fibers in the brain, spinal cord and optic nerves that creates lesions and CNS atrophy in both grey matter (GM) and white matter (WM) tissue. With the progression of plaques, carries nerve impulses along the nerves become slow, which cause the symptoms of MS.

Brain imaging is a promising field for the diagnosis of MS that not used only to raise percentage of diagnosis, but also monitoring of disease progression and treatment efficacy. Since MS plaques are visible on brain tissue and anatomy, experts are used magnetic resonance (MR) images which show a good discrimination between tissues. Another characteristic of MR images is imaging of members of body in axial, coronal and sagittal directions. Conventional MR images such as T1-weighted (T1), T2-weighted (T2), proton density-weighted (PD) and fluid attenuated inversion recovery (FLAIR) are sensitive to lesions and show them with different intensity to peripheral tissues. Also intensity of MS lesions and brain tissues is different in various MR sequences [2]. Accordingly, the use of multispectral images is necessary to achieve

an efficient algorithm. Lesions are often classified into three main groups based on their intensity under different MR sequences: T2 hyperintense lesions, gadolinium (Gd)-enhanced lesions and black holes [3].

Segmentation methods are mainly dependent on characteristics, application and quality of MR images. Imaging parameters, noise and artifacts, partial volume effects, non-uniform intensity, the patient movement during imaging and differences in the topological architectures of human brain, among the reasons for segmentation of MS lesions in MR images is difficult.

Survey papers in the field of automatically segmentation of MS lesions; have presented different categories of MS lesion segmentation approaches. Reference [1] suggested dividing the algorithms into two categories: supervised and unsupervised methods. Supervised group use prior knowledge such as atlas registration and manual segmentation (based on training) for the detection of MS lesions (i.e. Bayes classifiers with labeled maximum likelihood estimators, KNN and artificial neural networks (ANN)) and unsupervised group is divided into those techniques that use tissue segmentation to obtain the lesions and those that use only the lesion properties for the segmentation (i.e. Bayes classifiers with unlabeled maximum likelihood estimators or the fuzzy C-means (FCM) algorithms).

Another point of view, Classification methods can be grouped into two main approaches: class-based and outlier-based methods [4]. In the class-based methods, MS lesions are classified in a separate class along the same as three brain tissues [5]. In the outlier-based methods, brain tissues are assigned to three classes while MS lesions are delineated as outliers [6]. Since the number of voxels of the lesions class is much less than voxels belonging to other tissues, the estimated probability density function for the lesions class, is not as accurate as those of the other classes. As a result, it is expected that the outlier-based methods generate more accurate segmentation of the MS lesions.

In [4], some key individual classification methods are compared in terms of accuracy, time calculation, memory storage and computational complexity. Based on this comparison, there is a trade-off between accuracy and time calculation. Essentially, high precision spends more time. According to the evaluation proposed methods, in order to reach to an efficient and practical approach, it is necessary to consider a few points: the use of multispectral MR images, spatial features, manual segmentation and atlas registration. Moreover, segment lesion as outliers.

In order to consider above assumptions, it's necessary to present a unified approach of supervised and unsupervised methods. In the present study, we developed and implemented HMRF unsupervised method (that has been reported as the most successful method for segmentation of brain tissues [7]) to classify three main brain tissues on the high resolution 3D images. This method using of multi-channel images and without need expert segmentation, provides high-precision results in the field of brain tissues segmentation and since the inherently uses spatial features, the error due to noise and non-uniform intensity of tissues is reduced. We obtained initial segmentation of brain tissues thanks to a priori registration with the statistical atlas and without considering a separate class for MS lesions in the segmentation step, lesions are delineated as outlier at the post-processing step. On the other hand, we implemented SVM and KNN methods as training-based approaches to using real characteristics of the brain tissues and lesions. Finally, by combining the results of three segmentation methods achieved acceptable results. In this study, the focus is only on the classification of lesions have surrounded by WM (WML) from FLAIR sequences. We also validated the WML classification using quantitative analyses.

1 Material and Methods

a. Patients and MR images

The datasets were obtained from the MS lesion segmentation grand challenge (Medical Image Computing and Computer Assisted Intervention, MICCAI 2008) that has provided MR brain images for validating MS lesions segmentation technique (http://www.ia.unc.edu/MSseg/). The MRI data (with different volumes of MS lesions) were acquired on a 3T Siemens MRI scanner by the Children's Hospital Boston (CHB) and the University of North Carolina (UNC). In total, the brain MRI volumes of 45 MS patients were randomly divided into training sets (10 from each source), and testing sets (15 from CHB, 10 from UNC). The training sets also include expert lesion segmentation. But the lesion segmentation on the testing data obtained by the CHB and the UNC experts are not available to the public. Therefore, we just exploited the training sets to evaluate the method.

For all cases, the datasets contained the same number of high resolution images: a T1-w, a T2-w and a FLAIR image that are co-registered and re-sampled to $512 \times 512 \times 512$ with voxel dimensions of $0.5 \times 0.5 \times 0.5$ mm3. In this study, the segmentation method has been applied only to the 20 slices of MR images.

b. Automated Segmentation of MS Lesions

The six major components of the proposed segmentation technique are: (1) image pre-processing, (2) segmentation of brain tissues by HMRF (3) detection of lesions as outliers, (4) segmentation of WML by KNN, (5) segmentation of WML by SVM and (6) combining classifiers.

c. Image pre-processing

Image pre-processing will has a significant impact on the accuracy of the segmentation results. The image pre-processing includes co-registration, Image cropping, Skull-stripping, intensity non-uniformity correction, noise reduction and intensity normalization. It is important that the steps be performed respectively because it affects to improve image quality. MR sequences of MICCAI 2008 dataset are already co-registered. This means that a same voxel in the different sequences represents the same location in the brain.

In order to reduce the computational complexity, removed the number of voxels belonging to the background and decreased the image size to 390×290. The majority of Skull-stripping techniques extract the intracranial space from the image. For this purpose, we have applied automated brain extraction algorithm to the T2 images by exploiting the brain extraction tools (BET) in the MRIcro software [8]. Following that skull stripped T2 image was used to generate the mask which was applied to the T1 and FLAIR images.

Difference in intensity of same biological tissues that generated by the bias field is called image in-homogeneities. In our case, we estimated and corrected these in-homogeneities with the N3 method proposed in [9]. Also, to reduce noise without blurring small morphological details an anisotropic diffusion filter was applied [10] and finally the intensity profiles of the images were normalized (range from 0 to 255) using the decile based piece-wise linear transformation technique [11].

d. Segmentation of Brain Tissues by HMRF

Hidden Markov random fields have been suggested in image processing in order to model neighborhood and spatial interactions. Methods relying on MRF define the image as a set of N discrete sites (N is number of voxels) in which each site represents a voxel connected to its neighboring. Following Morkovian properties, assigning a label to each site only depends on label of its neighborhood set. In this study, we used HMRF algorithm to segment brain tissues. The FLAIR sequence provides a better distinction between lesions and normal tissue but the boundary between tissues has low resolution. Accordingly, tissues have been segmented only base on the features extracted from the T1 and T2 sequences [7].

Elimination of partial volume artifacts is one of the complexities of the MR images segmentation. In this case, a voxel may be composed of more than one tissue type. Partial volume problems arising from low resolution images or surface area is intended for a voxel that can be influence on the statistical properties such as mean and variance. To address this problem we have considered a separate class for voxels that are in the border areas between the two tissues [12]. In this approach, we defined two main types of classes: pure tissues which are assumed to follow a Gaussian mixture distribution and included WM, GM and cerebrospinal fluid (CSF) classes and partial volume classes which are defined as proportion between GM and CSF as well as WM and GM. While other interactions are excluded due to their slight influence.

MR images segmentation is performed in the following hierarchical procedure: (1) the probability of each voxel to belonging to the different classes is first initialized thanks to the a priori registration with the MNI atlas. At this stage, first a global affine transformation between the patient's T1 image and the atlas's template is estimated using mutual information and following that an initial segmentation of brain tissues is obtained using the module in SPM8 [13]; (2) The initial parameters of each class (mean and variance) are computed from the voxel intensities. Noting that the parameters of the partial volume classes are computed as a proportion of the pure tissue parameters, while the parameters of the background class are obtained as a fraction of the CSF parameters [12]; (3) Using current parameter set the labels of each voxel estimated by MAP estimation. This means that the label assigned to each voxel is updated based on label of its neighboring voxels [14]; (4) Based on labeled image obtained from the previous step, a new parameter set is estimated for each class using EM algorithm; (5) Steps 3 and 4 are repeated until a termination condition is achieved.

e. Detection of MS Lesions as Outliers

At the tissues segmentation stage, a class for lesions was not assigned. Therefore, Lesions incorrectly segmented in another classes due to intensity similarity with normal tissues. In this case, MS lesions are detected as outliers that do not follow the intensity Gaussian model. That means, distance between the intensity vector of outlier voxels and the mean vector of each class is greater than a threshold.

Lesions appear as hyperintense signals in FLAIR images. Moreover, GM voxels have the highest intensity in comparison with the other normal tissues in these images but its intensity is lower than the MS lesions. As a result, a significant difference between normal tissues and MS lesions appears in FLAIR images. Therefore lesion should be segmented as a GM-based class (pure GM or partial volume) or WM (black holes) that should always surrounded by WM tissue.

The aim of this step is apply a threshold on FLAIR images to find the candidate regions for lesions Class. First we assume GM intensities follow the Gaussian distribution. Also we assume that lesions are hyperintense outliers of GM class. According to these assumptions, a threshold on FLAIR image is defined as follows [15]:

$$T = \mu_{GM} + \alpha\sigma_{GM} \tag{1}$$

That μ_{GM} and σ_{GM} are respectively the mean and standard deviation of GM on FLAIR images and α is an experimental parameter used to determine the outliers and set to 2 [16]. To estimate tissue parameters, we first applied GM mask that obtained in HMRF segmentation to FLAIR image and then calculated them by using the proposed method at the [17].

The application of this threshold on the FLAIR images help us to detect lesions have at least a voxel with intensity higher than the threshold. But due to intensity non-uniformity of lesion voxels, we enhanced the contrast in the FLAIR image thanks to morphological operations before plying the threshold [16].

After thresholding, we obtained an initial lesion mask while other hyperintense artifacts are included (false positive). In other hand the MS lesions include voxels outside the mask (false negative). Therefore, this mask must be refined, based on appearance and spatial characteristics of the MS lesions. For this purpose, we defined a set of rules that are true for WML as follow [15]:

- o Lesions are mostly classified in WM and GM-based classes (pure GM and partial)
- o Lesions have surrounded by WM
- o Lesions should not be present between ventricles
- o Lesions should be of a minimum size.
- o By applying these rules on the FLAIR images, the remaining regions will be introduced as MS lesions.

f. Segmentation of WML by KNN

In this section, we proposed a supervised segmentation method based on KNN classification that has been introduced in [18]. In this approach, a new voxel image is classified by the majority class of the K learning samples (K=50) that are closest in terms of Euclidian distance to it. However, instead of assign one class to the voxel, determine the probability being a lesion per voxel by taking the number of lesion voxels among the k neighbors. As a result, a lesion probability map is constructed for every test image. Subsequently the map is threshold to derive a binary segmentation of the lesions. We defined an optimal threshold of 0.4 to apply on all probabilistic segmentations of the testing sets.

g. Segmentation of WML by SVM

SVM classifier has provided satisfactory results as a binary classification task like the one in our study (normal tissues/MS lesion) [19]. Initially a set of training samples that manually segmented by expert used to build a classification model via SVM. Then the SVM model is used to perform the voxel-wise segmentation. This means, lesion rating for each voxel (likelihood of being lesion) is estimated by the generated SVM classifier where each voxel is assigned with values in the range [-1, 1]. If this value is close to -1, probabilities that a voxel belongs to tissues class is more than lesion class and if it close to 1 more likely to belong to the lesion class. Finally the output of SVM is binarized by an optimal threshold of 0.8 to produce the labels for MS lesions.

It should be noted, because of the large number of voxels in the training sets only 30% of lesion voxels and 5% of tissues voxels are randomly selected as the training points. Also the feature space have been used in supervised methods (KNN and SVM) are included voxel intensity of FLAIR Images and voxel location in the brain that is uniquely defined by the x, y and z coordinates. These features further are normalized to have zero mean and variance of one.

h. Combining Classifiers

Numerous experiments have been conducted on combining classifiers [20]. The main objective of designing different classification schemes is to achieve the best classification. Considering the situations (different classifiers with different features) we developed Majority Vote rule to combine results of three classifiers [21]. The Maximum rule counts the votes for each class over the input classifiers and selects the majority class. In general, at each value of X a majority vote classifier consisting of votes from rules $h_1,h_2,...,h_b$ is defined as follows:

$$C(X) = \arg\max_i \sum_{j=1}^{B} w_j I(h_j(X) = i)$$
(2)

Where $w_1,w_2,...,w_b$ are weights of classifiers 1,2,...,B that sum to 1 and I is an indicator function is define as follows:

$$I(y) = \begin{cases} 1: & \text{if } y = \text{true} \\ 0: & \text{if } y = \text{false} \end{cases}$$
(3)

We assume equal weights for all classifiers in which case all the weights w_i set to 1/B.

2 Validation

We have used K-fold cross-validation method to evaluate performance of proposed method. In this approach, the dataset equally is divided into k subsets. Then for each of k experiments, k-1 folds for training and the remaining one for testing are used. So that the all samples in the dataset are eventually used for both training and testing. Finally, the accuracy of proposed method is obtained as the average of k separate estimates.In our problem, we have k=4 subsets.

We have implemented the segmentation method in Matlab-code using a dual core processor 2.1 GHz and 3 GB RAM. Specifically, we used libSVM in Matlab to develop SVM classifier [22]. The kernel function has been used in our application is Gaussian radial basis function (RBF).

i. Evaluation measures

Various measures are used to evaluate the proposed methods for the segmentation of the MS lesions. The Lesions have detected by the expert were considered as the reference lesion classification (ground truth). The automatic segmentation results and ground truth can be compared by either comparing each voxel in each lesion (voxel to voxel), or using the total lesion load (lesion-to-lesion). In both cases, two-class classification model for image segmentation is implemented in which voxels and lesions can be classified as a true positive (TP), false positive (FP), true negative (TN) or false negative (FN). In our problem, we assigned a class to lesions and a class to other regions of image (including brain tissues and background voxels).

The quantitative metrics used for the evaluation included dice similarity coefficient (DSC), absolute volume difference percent (Vol_Diff) and average symmetric surface distance (Avg_Dist) defined as:

$$DSC = \frac{2 \times TP}{2 \times TP + FP + FN} \tag{4}$$

$$Vol\_Diff = (abs\ (reference\ volume - segmentation\ volume) / *100 \tag{5}$$

$$Avg\_Dist = (\sum_{x \in \partial(Ref)} \min_{y \in \partial(Seg)} d(x, y) + \sum_{x \in \partial(Seg)} \min_{y \in \partial(Ref)} d(x, y)) / (card(Seg) + card(Ref)) \tag{6}$$

Here, ∂(Ref) and ∂(Seg) represent sets of border voxels of the ground truth (Ref) and segmented lesions (Seg) and the term card(Ref) and card(Seg) denote the number of border lesion voxels. For each voxel (x) along one border, the closest voxel (y) along the other border in term of Euclidean distance (d(x,y)) is determined. The average of all these minimum distances for border voxels from both reference and segmentation gives the average symmetric surface distance. Vol_Diff and Avg_Dist for a perfect segmentation should be close to 0 and DSC conformity index should be close to 1. Practically, a DSC value greater than 0.7 indicates a good segmentation performance.

In addition, the ideal evaluation of the MS lesions segmentation methods should be based on multi-raters (the variable ground truth) using techniques such as the simultaneous truth and performance level estimation (STAPLE) [23]. For evaluation of the estimated lesions compared with the combined STAPLE segmentation the specificity, sensitivity, and positive predictive value (PPV) were calculated. PPV value provides a good measure combining both sensitivity and specificity. A good segmentation system should have high sensitivity and specificity values.

j. Results

The HMRF method classified the brain tissues into six different classes (Figure 1). The aim of this procedure is to obtain tissue masks that are used in the lesions segmentation step.
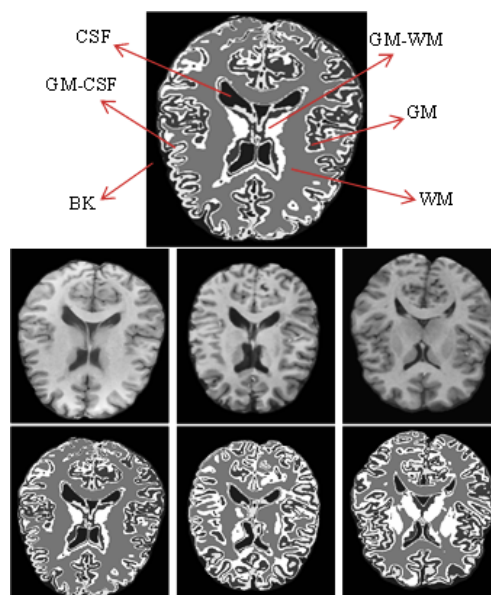
Figure 1: Tissue segmentation using HMRF: Top row: T1 images of some cases, bottom row: segmented images.

In Figure 2 an example of the detected lesions; as outliers in the FLAIR images, have been shown. On the other hand, SVM and KNN classifiers in a two–class problem have been applied to detect MS lesions from the FLAIR images.
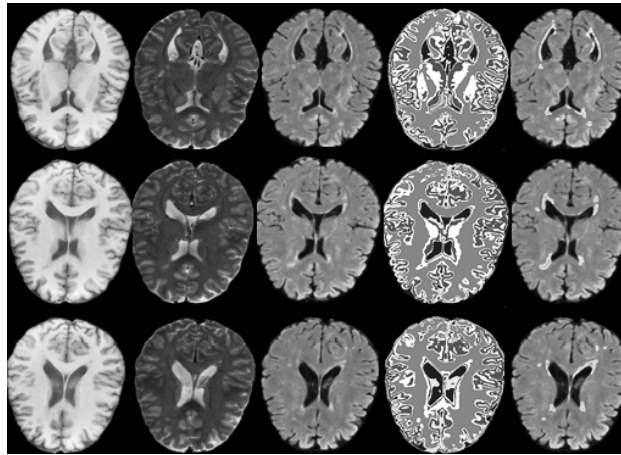
Figure 2: HMRF classification at various cross-sections of the CHB_Case02. First column: T1; second column: T2; third column: FLAIR; fourth column: segmented tissues; and fifth column: segmented lesions.

Figure 3 shows the results of lesion segmentation based on supervised approaches. Finally, the obtained segmentations of the three classifiers are combined to achieve accurate results.
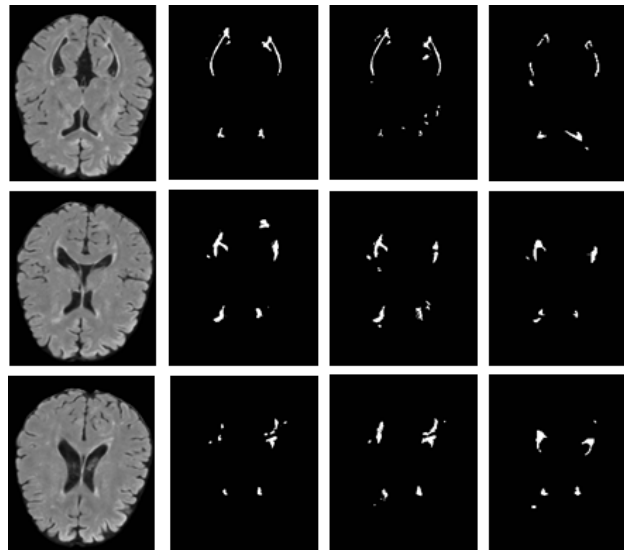
Figure 3: Supervised classification at various cross-sections of the CHB_Case02. First column: FLAIR image; second column: lesions segmentation by KNN classifier; third column: lesions segmentation by SVM classifier; fourth column: expert segmentation.

The final results of proposed methods are demonstrated in Figure 4.
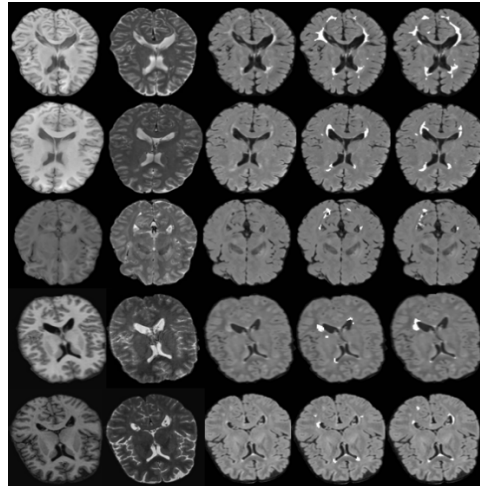
Figure 4: Automated segmentation of MS lesions at five cases from the MICCAI dataset. First column: T1; second column: T2; third column: FLAIR; fourth column: expert segmentation; and fifth column: segmented lesions by proposed method.

In Some cases with low quality of FLAIR images, the points with high signal intensity are observed to scattered noise within WM (e.g. UNC-case05 و UNC-case09). These points due to having the same intensity with MS lesions are misclassified as lesions. Since, lesion segmentation step in HMRF approach only performed base on the intensity images, segmentation results of this approach provide less accurate than the supervised methods for this cases. Also, in reference images of some cases, experts have determined the voxels as MS lesions, which not included the characteristics of the two types of T2 hyperintense and black hole lesions (such as CHB-case01 and CHB-case10). In fact, the voxels have similar intensity with WM in FLAIR and T1 images. Therefore, it is expected that the detected lesions have been Gd-enhanced lesions. These lesions show an increase in intensity compared to WM on T1 images after injection with gadolinium. Since the dataset is not included the Gd-enhanced T1 images, the detection of this type of lesions is difficult.

Unlike HMRF approach in which the regions between the ventricles are firstly detected as MS lesions (and are removed of lesions class at the post-processing step), the supervised methods typically not segmented these regions in lesions class thanks to use location information of lesions. But as an advantage of HMRF, the details of image segmented by HMRF are much more than other segmentation methods. As a result, HMRF shows a better performance of the diagnosis of scattered MS lesions. Tissues segmentation also helps us to obtain the mask of brain tissues and by applying those on the MR images achieved three objectives: detecting the voxels of the tissues class that have similar intensity with MS lesions, defining region of interest for identify lesions occurring in WM and segmenting tissues with respect to the effects of partial volume.

It can be concluded that by understanding the advantages and limitations of the methods, can be represented a combining approach to achieve more accurate in the diagnosis of MS lesions. Note that cannot be represented definite results of the performance of the segmentation techniques that be true for all type of MR images and MS lesions. Because the characterizes have been defined for types of MS lesions may not be true in some regions of MR images, but an expert based on personal experiences has recognized these regions as MS lesions

k. Quantitative Evaluation

The results of comparison between the automated segmentation and the ground truth are presented in Table 1.

Table 1. Results obtained on the public dataset of MICCAI.

	HMRF			KNN			SVM			Merge results		
	Vol Diff (%)	Avg Dist (mm)	DSC (%)	Vol Diff (%)	Avg Dist (mm)	DSC (%)	Vol Diff (%)	Avg Dist (mm)	DSC (%)	Vol Diff (%)	Avg Dist (mm)	DSC (%)
Average all dataset	44.44	7.85	76.5	37.96	7.24	77.43	35.8	7.55	79.13	35.73	7.93	80.03

Table 1 provides detailed quantitative metrics, DSC, Vol_Diff and Avg_Dist for the three classifiers and combined model. In order to facilitate the comparison, a bar chart of Dice coefficient for the three classifiers is shown in Figure 5.
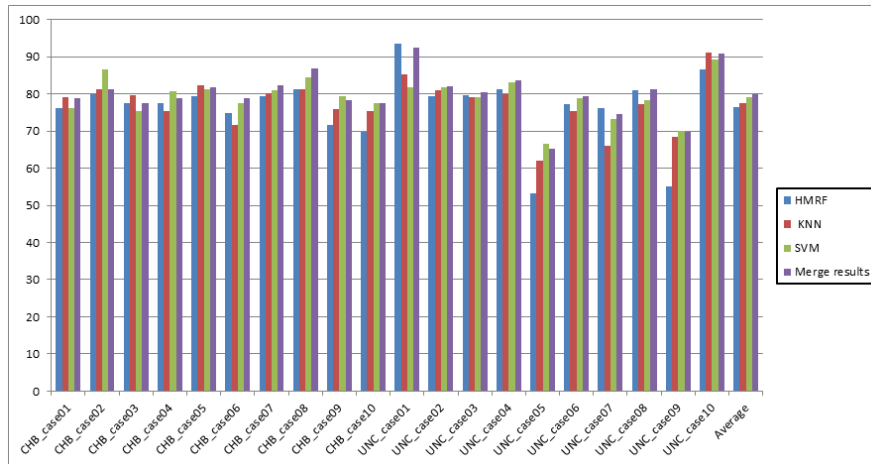
Figure 5: Bar chart for Dice coefficient.

Our technique received a DSC average value of 76.5, 77.43 and 79.13 percent for HMRF, KNN and SVM, respectively. We also calculated the DSC value for combined model. This improved the DSC value to 80.03 percent. The results indicate that the accuracy of MS lesions segmentation can be increased by combining the segmentation results of the three classifiers.

Note the cases with significant different lesion load can bias the results. The results of volumetric comparison of lesions between the automated segmentation and the ground truth are presented in Table 2.

Table 2. DSC values in MR images with different volumes of lesions.

Patient category	Number of cases	DSC (%)
Small lesion load	6	77.78
Moderate lesion load	9	80.69
Large lesion load	5	81.73

For the patients with large lesion load, we reached to average value 81.73 for DSC which is more than those patients with small and moderate lesion load.

In Table 3 the segmentation results of our method were also compared with combined STAPLE segmentation. All binary segmentations of the 10 UNC images have been compared with manual segmentations of the two raters: a UNC rater and a CHB rater.

Table 3. Results of the segmentation method by STAPLE.

UNC dataset	STAPLE		
	Specificity	Sensitivity	PPV
UNC_case01	0.999	0.6092	0.9545
UNC_case02	0.9972	0.5912	0.8741
UNC_case03	0.9995	0.4096	0.9448
UNC_case04	0.9995	0.4638	0.9015
UNC_case05	0.9871	0.1745	0.3175
UNC_case06	0.9937	0.4972	0.8283
UNC_case07	0.9953	1	0.4853
UNC_case08	0.9968	0.7734	0.8537
UNC_case09	0.9879	0.8977	0.6037
UNC_case10	0.9987	0.5999	0.8975
Average	0.9955	0.6016	0.7661

The average execution time in seconds was computed for all cases in dataset. According to Table 4, the total computational time for complete segmentation, including the preprocessing, feature extraction and lesions detection is 44.25 min that took considerable time. This time can be reduced using algorithms based on parallel computation.

Table 4. Average execution time of the method for 20 slices of MR images.

Steps	Time (second)
Pre-processing	355
Feature extraction	68
HMRF tissue segmentation	1470
Lesion detection by tissue mask	10
KNN classification	672
SVM classification	72
Merge results	8
Total	2655 (44.25 min)

Quantitative comparison among the approaches is a difficult task due to the variability in the datasets and evaluation measures. Table 5 provides a qualitative comparison of the DSC Coefficient obtained by the MS lesions segmentation approaches.

Table 5. DSC values for the proposed method and the other methods.

Segmentation method	MR images	Number of samples	DSC (%)
EM+MRF [6]	T1, T2, PD	50	51
ANN [24]	T1, T2, PD	29	60
Parzen windows [25]	T2, PD, FLAIR	23	78
Bayes+AMM+MRF [26]	FLAIR	20	75.04
Simulated annealing +MRF [5]	T1, T2, PD	10	71
FCM [27]	T1, T2, FLAIR	10	77
Proposed method	T1, T2, FLAIR	20	80.03

We have also provided a comparison among the approaches that have used of MICCAI dataset in Table 6.

Table 6: Comparison of the results of MS lesions segmentation on the MICCAI dataset.

Segmentation method	Vol Diff (%)	Avg Dist (mm)	Specificity	Sensitivity	PPV
KNN [18]	46.9	7.8	0.9970	0.4519	0.9143
EM+GMM [16]	86.5	8.2	0.9895	0.3583	0.6004
AdaBoost [28]	133.4	13.2	0.9879	0.2893	0.5093
Bayes [29]	174.6	22.2	0.9476	0.2984	0.4221
Proposed method	35.7	7.93	0.9955	0.6016	0.7661

Note that even a few cases with low quality images, have a significant negative effect on the average results of the proposed method.UNC-case09 and UNC-case05 with low quality of FLAIR images have decreased the average PPV value of the proposed methods.

3 Conclusion

We have presented and implemented a unified and automated approach for classifying MR brain images in MS. The aim of this unified approach is to combine the segmentation results from supervised and unsupervised methods for creating effective MS lesions segmentation. The proposed automated segmentation technique was assessed quantitatively for WML classification with the use of quantitative metrics on MICCAI dataset. The results of the automatic lesion segmentation were compared with lesion delineations by experts, showing a high total lesion load correlation. In the future, we will focus on studying the atrophy of brain and spinal cord, which is an important part of MS pathology.

REFERENCES

[1].   Lladó, X., et al., *Segmentation of multiple sclerosis lesions in brain MRI: A review of automated approaches*. Information Sciences, 2012. 186(1): p. 164–185.

[2].   Hashemi, RH., WG. Bradley and CJ. Lisanti, *MRI: the basics*. 3td edition, Philadelphia: Lippincott Williams and Wilkins, 2004. 400.

[3].   García-Lorenzo, D., et al., *Review of automatic segmentation methods of multiple sclerosis white matter lesions on conventional magnetic resonance imaging*. Medical Image Analysis, 2013. 17(1): p. 1–18.

[4].   Mortazavi, D., A. Z. Kouzani and, H. Soltanian-Zadeh, *Segmentation of multiple sclerosis lesions in MR images: a review*. Neuroradiology, 2012. 54(4): p. 299–320.

[5].   Subbanna, N., et al., *MS lesion segmentation using Markov Random Fields*. Medical Image Analasis Multiple Sclerosis, 2009: p. 15–26.

[6].   Leemput, KV., et al., Automated segmentation of multiple sclerosis lesions by model outlier detection. Medical Imaging, IEEE Transactions on, 2001. 20(8): p. 677–688.

[7]. Zhang, Y., M. Brady and, S. Smith, *Segmentation of brain MR images through a hidden Markov random field model and the expectation-maximization algorithm*. Medical Imaging, IEEE Transactions on, 2001. 20(1): p. 45–57.

[8]. Smith, SM., *Fast robust automated brain extraction*. Human Brain Map, 2002. 17(3): p. 143–155.

[9]. Led, JG., AP. Zijdenbos and, AC. Evans, *A nonparametric method for automatic correction of intensity nonuniformity in MRI data*. Medical Imaging, IEEE Transactions on, 1998. 18(1): p. 87–97.

[10]. Perona, P. and, J. Malik, Scale-space edge detection using anisotropic diffusion. Pattern Analysis and Machine Intelligence, IEEE Transactions on, 1990. 12(7): p. 629-639.

[11]. Nyúl, LG., GK. Udupa and, X. Zhang, *New variants of a method of MRI scale standardization*. Medical Imaging, IEEE Transactions on, 2000. 19(2): p. 143-150.

[12]. Tohka, J., A. Zijdenbos and, A. Evans, *Fast and robust parameter estimation for statistical partial volume models in brain MRI*. NeuroImage, 2004. 23(1): p. 84 – 97.

[13]. Ashburner, J., et al., *SPM8 Manual*. 2013.

[14]. Patts-Shattuck, DW., et al., *Magnetic resonance image tissue classification using a partial volume model*. NeuroImage, 2001. 13(5): p. 856 – 876.

[15]. Cabezas Grebol, M., PhD. Thesis, *Atlas-based segmentation of multiple sclerosis lesions in magnetic resonance imaging*. de Girona University, Spain, 2013.

[16].   Souplet, J., et al., *An automatic segmentation of T2-FLAIR multiple sclerosis lesions*. Multiple Sclerosis Lesion Segmentation Challenge 2008: p. 1–11.

[17]. de Boer, R., et al., *White matter lesion extension to automatic brain tissue segmentation on MRI*. Neuroimage, 2009. 45(4): p. 1151-61.

[18]. Anbeek, P., K. Vincken and, K. Viergever, *Automated MS-lesion segmentation by k-nearest neighbor classification*. Multiple Sclerosis Lesion Segmentation Challenge 2008: p. 1–8.

[19]. Laoa, Z., et al., *Computer-assisted segmentation of white matter lesions in 3D MR images, using Support Vector Machine*. Acad Radiol, 2009. 15(3): p. 300–313.

[20]. Duin, RPW. and DMJ. Tax, *Experiments with classifier combining rules*. Lecture Notes in Computer Science, 2000: p. 16-29.

[21]. James, G., PhD. Thesis, *Majority vote classifiers: theory and applications.* Stanford University, 1988.

[22]. Chang, C. and, C. Lin, *LIBSVM: a library for support vector machines*. 2001.

[23]. Warfield, SK., KH. Zou and, WM. Wells, *Simultaneous truth and performance level estimation (staple): an algorithm for the validation of image segmentation*. Medical Imaging, IEEE Transactions on, 2004. 23(7): p. 903–921.

[24]. Zijdenbos, AP., R. Forghani and, AC. Evans. *Automatic ''pipeline'' analysis of 3-D MRI data for clinical trials: Application to multiple sclerosis*. Medical Imaging, IEEE Transactions on, 2002. 21(10): p. 1280–1291.

[25]. Sajja BR., et al., *Unified approach for multiple sclerosis lesion segmentation on brain MRI*. Annals of Biomedical Engineering, 2006. 34(1): p. 142–151.

[26]. Khayati, R., et al., *Fully automatic segmentation of multiple sclerosis lesions in brain MR FLAIR images using adaptive mixtures method and Markov random field model*. Comput Biol Med, 2008. 38(3): p. 379–390.

[27]. Shiee, N., et al., *A topology-preserving approach to the segmentation of brain images with multiple sclerosis lesions.* NeuroImage, 2010. 49(2) : p. 1524–1535.

[28]. Morra, J., et al., *Automatic segmentation of MS lesions using a contextual model for the MICCAI grand challenge*. Multiple Sclerosis Lesion Segmentation Challenge 2008: p. 1–7.

[29]. Scully, M., et al., *3D segmentation in the clinic: a grand challenge II at MICCAI 2008 –MS lesion segmentation*. Multiple Sclerosis Lesion Segmentation Challenge 2008: p. 1–9.

Measurement of Arterio-Venous Ratio for Detection of Hypertensive Retinopathy through Digital Color Fundus Images

[1]Anju Rani and [2]Deepti Mittal
[1]Department of Electrical and Instrumentation Engineering, Thapar University, Patiala, India
[1]anju.yaduvanshi@yahoo.com; [2]deepti.mittal@thapar.edu

ABSTRACT

Hypertensive retinopathy is a retinal vascular damage caused by high blood pressure which results in loss of vision. In the present work, effort has been devoted to enhance and segment the retinal vasculature which is required to calculate its anatomical characteristics such as width, length for the quantitative measurement of arterio-venous ratio (AVR). Enhancement of the retinal fundus images is done using top-hat transform and segmentation of the vessels using iterative thresholding. The performance of the proposed method is tested on 50 digital fundus images of publicly available MESSIDOR dataset. The hypertensive retinopathy can be measured quantitatively by detecting the decrement in the ratio of width of retinal artery-vein to that of the normal images. The arterio-venous ratio obtained by applying the proposed methodology was found to be 0.62-0.735 in normal cases and 0.203-0.495 in case of patients suffering from hypertensive retinopathy on MESSIDOR dataset which was not performed earlier. This measurement of arterio-venous ratio will be further helpful to identify the stages of hypertensive retinopathy.

Keywords: Hypertensive retinopathy; fundus image; arterio-venous ratio; arterio-venous nicking

[13]   **Introduction**

The abnormality of retina caused by high blood pressure is called hypertensive retinopathy. When the blood pressure is too high, the retina's blood vessel walls may thicken. This may result in narrowing of the vessels, which restricts blood to reach up to retina. Hypertensive retinopathy (HR) causes various changes in the retinal blood vessels such as leakage from blood vessels, and swelling in other parts of the retina. Figure1 (a) shows major parts of retina such as optic disc, macula, artery, vein while Figure1 (b) represents various effects of HR such as vascular wall changes, flame-shaped hemorrhages, cotton-wool spots, yellow hard exudates, and papilloedema [1,2]. Prolonged high blood pressure can cause damage to the retina's blood vessels and limit the retina's function, and can also put pressure on the optic nerve that may lead to complete vision loss. Worldwide, hypertensive retinopathy is now a leading cause of disability and mortality. Its prevalence is expected to reach 30% worldwide by 2025. Wong *et al.* [2] surveyed that hypertensive patients were 50–70% more likely to have retinal hemorrhages and micro aneurysms, 30–40% more likely to have focal arteriolar narrowing and 70–80% more likely to have arterio-venous (AV) nicking than normal individuals. Patients suffering with diabetes as well as hypertension greatly increases risk of vision loss. The automated detection of vascular changes of blood vessels is a challenging task [3]. In the present work, effort has been devoted to enhance and segment the retinal vasculature which is

required to calculate its anatomical characteristics such as width, length for the quantitative measurement of arterio-venous ratio (AVR).
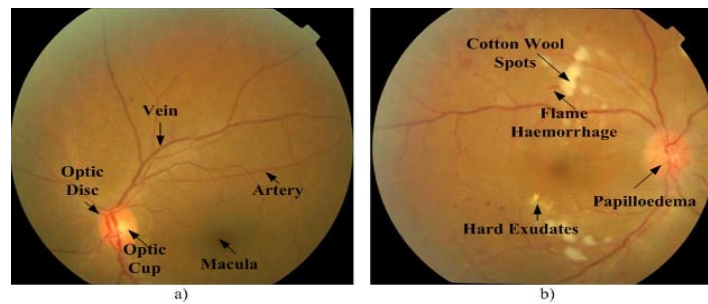
Figure 1. Hypertensive retinopathy on digital fundus image: a) normal fundus image, b) fundus image showing effects of hypertensive retinopathy.

[14]Related Work

Narasimhan *et al.* [4] presented a method for blood vessel detection using median filter and top hat transform on 76 images of VICAVR database and 25 clinically acquired retinal fundus images. Inspite of using large dataset, grading has not been done in their work. Manikis *et al.* [5] work was based on hessian based vessel segmentation technique along with thresholding. It was tested on two different standard databases DRIVE, STARE. The limitation of their work was that optic disc detection technique has not been discussed properly. Agurto *et al.* [6] developed automated vessel segmentation method based on a multi-scale linear structure enhancement and the second order local entropy thresholding. Calculation of AVR is done on the six widest (major) vessels for each category on 74 clinically acquired images. The limitation of their work was that the AVR calculation has been done only on region (0.5-1) optic disc diameter (DD) which may give inappropriate results according to them. Khitran *et al.* [7] work was based on classification of vessels as arteries and veins using new feature vector. They tested their method on 58 fundus images of VICAVR and 40 images of DRIVE database. The limitation of their work was that new computation method used for AVR calculation is not discussed properly. Ortiz *et al.* [8] proposed a method to calculate the AVR by using different techniques including Gabor wavelet, gradients and morphological operations. A set of 30 images was taken to test this algorithm. Their method gave undefined classifications for low illuminance images. Ruggeri *et al.* [9] presented an algorithm to enhance the image to highlight the vessel network, which is then traced by a vessel tracking algorithm. The method was tested on 50 clinically acquired images. It appeared that some vessels were missed by the tracing procedure and therefore gave faulty AVR and thus unsatisfactory performances.

On the basis of literature review, for the best result noise removal can be done by using gaussian kernel and enhancement can be carried out using top-hat transform. This insight is helpful to design a methodology to measure AVR ratio on the images of MESSIDOR dataset which has not been done earlier.

This paper is structured as follows: Section 3 outlines the materials used and describes the proposed method. Section 4 provides the experimental results of the proposed method and discussion on these results. Section 5 summarizes the key findings of the method and scope for future research.

Table 1. Performance Comparison of Hypertensive Retinopathy Detection.

Author (Year)	Image processing Methods	Database (Number of images)	AVR	
			Normal	Abnormal
Narasimhan *et al.* (2012) [4]	Median filter, Top hat transform	VICAVR(76) Clinically acquired(25)	0.6-0.7	0.24-0.49
Manikis *et al.* (2011) [5]	CLAHE, Hessian based vessel segmentation	DRIVE(40) STARE(20)	-	0.1-0.5
Agurto *et al.* (2014) [6]	Multi-scale linear structure, enhancement	Clinically acquired(74)	0.67	0.58
Khitran *et al.* (2014) [7]	Gabor wavelet, multilayered thresholding	VICAVR(58) DRIVE(40)	-	0.1-0.5
Ortiz *et al.* (2010) [8]	Gabor wavelet, Hessian matrix	Clinically acquired(50)	>0.6	< 0.6
Ruggeri *et al.* (2007) [9]	Vessel tracking method	Clinically acquired(50)	-	<0.57

[15]**Materials and Methods**

The retinal fundus images for the present study have been taken from open-source benchmark MESSIDOR database which is available online. MESSIDOR database were acquired by three ophthalmologic departments using a color video 3CCD camera on a Topcon TRC NW6 non-mydriatic retinograph with a 45 degree field of view. The images were captured using 8 bits per color plane at 1440×960, 2240×1488 or 2304×1536 pixels. The database contains a medical diagnosis for each image, but no manual annotations on the images, such as lesions contours or position.

The flowchart of the proposed method is presented in figure 2. Hypertensive retinopathy produces modifications in the retinal vessels; hence the present work is focused mainly on vessel enhancement and segmentation to characterize any morphological change in retina. Therefore, the main stages involved in this method are: (i) pre-processing step which mainly includes vessel enhancement process, (ii) post-processing step having vessel segmentation, binarization and optic disc detection as its main step, (iii) retinal tree labeling to perform characteristic measurements on composite image (iv) ROI detection to perform AVR calculation.

a. Pre-processing

The retinal fundus image consists of three channels; green, red, and blue. Amongst them, green channel is selected which has a better contrast and information than the other two channels.

Retinal blood vessels exhibit number of properties such as:

    i.   The blood vessels have small curvature.
    ii.   Vessels have lower reflectance than the background, so they appear darker.
    iii.   Vessel size may decrease when moving away from the optic disc, the width of a retina vessel may lie within the range of 2–10 pixels.
    iv.   The intensity profile may vary by a small amount from vessel to vessel.
    v.   The intensity profile of blood vessel has a Gaussian shape [10].

So the blood vessels are enhanced and segmented for further processing using following major steps:

3.1.1 Vessel central light reflex removal

Some blood vessels have a light streak (known as a light reflex) which runs down the central length of the blood vessel [4].The green plane of the fundus image is filtered to remove this brighter strip. So,

morphological opening is applied to the green channel using a three-pixel diameter disc as structuring element. The structuring element is selected such that it does not merge with the vessels that lie close to one another.

3.1.2   Background homogenization

The second step of preprocessing is background homogenization. A background intensity variation due to non-uniform illumination is associated with retinal fundus images. A 3x3 mean filter is applied to smooth occasional salt-and-pepper noise [11]. The image is smoothened further with a gaussian kernel with standard deviation of 0.5. A homogenized image in then obtained with reduced intensity variations in accordance to the green channel image.

3.1.3   Vessel enhancement

Vessel enhancement is the final pre-processing step to generate a new vessel enhanced image. It is performed initially by estimating the complementary image of the homogenized image [12,13]. It is further followed by morphological top-hat transformation of the complementary image. A disc structuring element of eight pixels radius was used in this step. The bright lesions i.e., optic disc, possible presence of exudates or reflection artifacts are removed while the dark features i.e., blood vessels, fovea, possible presence of micro aneurysms or hemorrhages remain in the image. The contrast between the vessels and other tissues are further improved after applying top-hat transform.
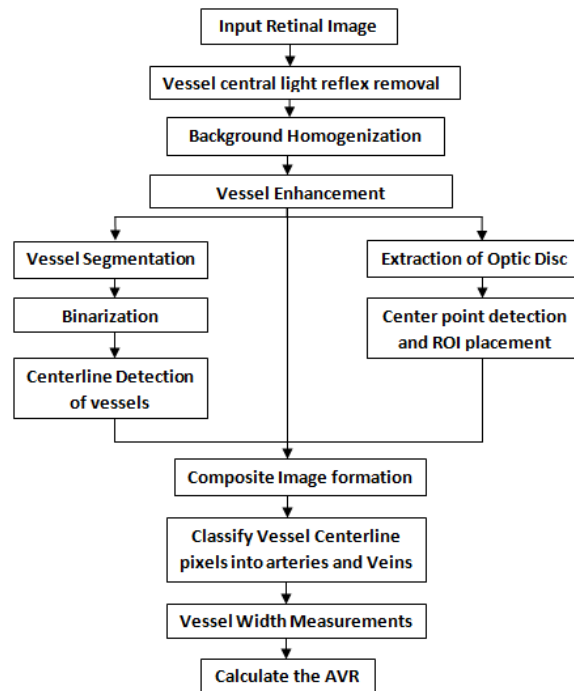

Figure 2. Flowchart of the proposed method

b. Post-processing

3.1.4   Vessel Segmentation

Classification of arteries and veins is an important step in HR detection. An iterative thresholding method for segmenting the blood vessel structure is applied for the binarization of the enhanced image [14,15,16]. Intensity variation and color information is used to classify the vessels as arteries and veins [17,18].

3.1.5   Optic disc detection and ROI Determination

Accurate detection of optic disc is necessary for determining the region of interest (ROI) so as to calculate the artery-vein ratio [6]. The center point of the optic disc is estimated by the automated method. The estimation is based on measurements obtained in the image and from the vessel segmentation. The target location is obtained by taking estimates in many locations in the image, ignoring those locations that are estimated to be far from the optic disc center [19]. The automated method detects the center of the optic disc and a circle with DD, is placed at this location. It was assumed that this circle corresponds to the optic disc outline in the image.

After the coordinates of the optic disc are located, two regions of interest are selected. Region A is between 0.5 and 1 DD from the optic disc center and region B is between 1 DD and 1.5 DD from the optic disc center. The two regions selected from optic disc center are shown in Figure 3(a). All analyses and evaluations performed in this work are based on measurements within region B. Region B is generally used for vessel measurements.
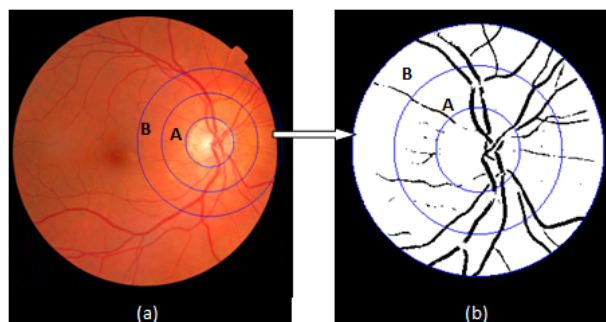
Figure 3. (a) ROI outlines marked on original image, (b) ROI in the binary image where region A is between (0.5 -1) DD and region B is between (1-1.5) DD.

3.1.6   Computation of AVR and Centerline detection

For computation of AVR, all the vessel width measurement has to be done initially. To calculate the vessel width from binary vessel mask, the center line for each vessel is obtained by morphological thinning operation. The thinning operation is performed till the vessel width equal to single pixel is obtained. This will provide center line for each vessel segment [8]. The vessel center line is combined with the filtered image and width is calculated for major six arteries and veins by measuring the perpendicular line that intersects the vessel edges [20]. Figure 4 represents the composite image obtained after the above process. The final width for each vessel segment is calculated as the median of all the widths of arteries and veins [6].

The AVR is computed by measuring Central Retinal Arterial Equivalent (CRAE) and Central Retina Venous Equivalent (CRVE). These two measurements of arterioles and venules are determined by Parr formulas

[21,22] and Hubbard [23] respectively. According to [23], the mean widths of arteries and veins segments within ROI are collected in two separate lists, namely "Arteriole" and "Venule". CRAE is computed as;
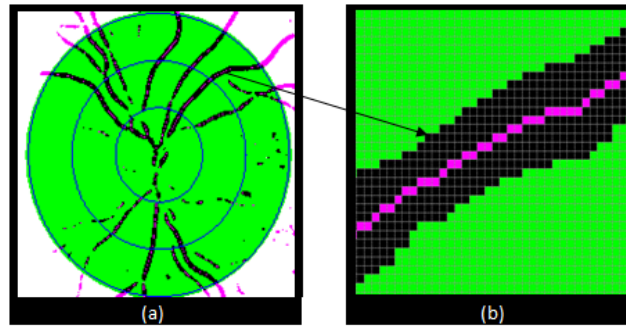
Figure 4. (a) Composite image of binarized and determined ROI image, (b) Image showing vessel width with centerline pixel.

$$CRAE = \sqrt{(0.87.X^2 + 1.01.Y^2 - 0.22.X.Y - 10.73)} \qquad (1)$$

Where Y is the median value of "Arteriole" and X is the value in the same list exactly before the median Y.

$$CRVE = \sqrt{(0.72.X^2 + 0.91.Y^2 + 450.02)} \qquad (2)$$

Where Y is the median of "Venule" and X is the value in the list exactly before Y. AVR is computed by dividing equation 1 and 2;

$$AVR = \frac{CRAE}{CRVE} \qquad (3)$$

3.1.7   Grading of Hypertensive Retinopathy

Keith and Wegner (1939) [24] have classified hypertensive retinopathy into following four grades. The change in vessel diameters is used to calculate AVR and it is significant in determining the presence of hypertensive retinopathy and grading its severity [25,26]. Table 2 shows various stages of HR along with AVR;

Table2. Grading of HR

Degree of HR	AVR	Symptoms
Normal Retina	0.667-0.75	None
Grade 1	0.5	Mild compression of venules
Grade 2	0.33	Compression of elevation of venules
Grade 3	0.25	Right angled crossing of vessels
Grade 4	< 0.2	All above symptoms along with papilledema

[16]**Experimental Results and Discussion**

The quantitative assessment of the proposed algorithm is done for hypertensive retinopathy detection. The algorithm was tested on 50 retinal images of MESSIDOR dataset. Images in figure 5 (a), (b) and (c) are randomly chosen retinal fundus images from MESSIDOR database that are used to demonstrate the results of proposed method.

The results of pre-processing are shown in figure 5 (d)-(i).The green channel images of the selected sample images are shown in figure 5 (d), (e) and (f) respectively. The output of homogenized image is complemented to get output image as figure 5 (g), (h) and (i) respectively. The enhancement of the processed images is then done by using top hat transform shown in figure 5 (j),(k) and (l) respectively. The contrast of the output obtained is then increased to get the enhanced image as shown in figure 5 (m), (n) and (o) respectively. The enhanced sample images are then binarized to obtain figure 6 (a),(b) and (c) respectively.

The width of arteries and veins is calculated on region B (1-1.5) DD as show in figure 3 (a), (b). The AVR is calculated after computing the width of arteries and veins as shown in figure 4 (a), (b). Table 3 displays statistical performance of the proposed method on MESSIDOR dataset. On the basis of Table 2, the retinal images can be divided into normal and abnormal images. The AVR obtained by the above mentioned methodology is 0.62-0.735 in normal cases and 0.203-0.495 in case of patients suffering from hypertensive retinopathy. Using the above algorithm 17 images out of 50 images was found to be normal images while 33 abnormal images detected the presence of hypertensive retinopathy.

In this research paper top-hat transform is used for the vessel enhancement and thresholding is used for segmentation of vessels. Optic disk detection is necessary for the correct estimation of ROI as well as for the computation of AVR.
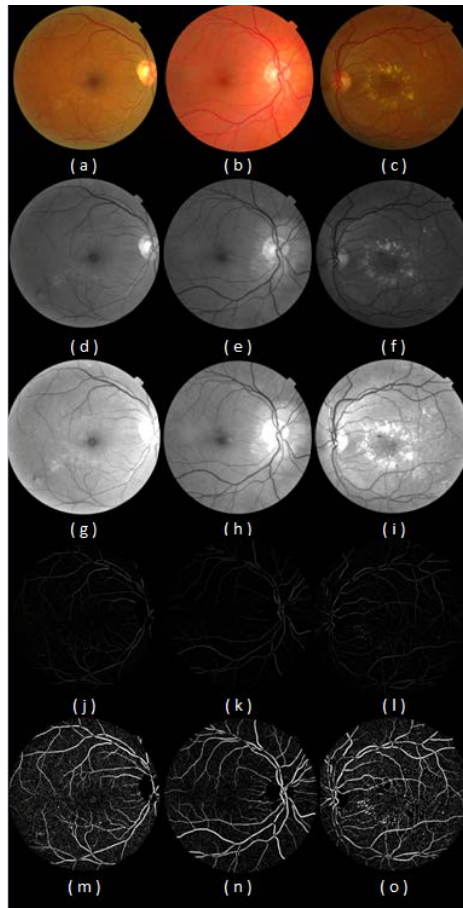
Figure5. Results of preprocessing of retinal fundus images: (a–c) original images from MESSIDOR dataset, (d–f) Green channel images, (g-i) complement of homogenized output image, (j-l) output images of top-hat transform, (m-n) enhanced images of top-hat transform outputs.
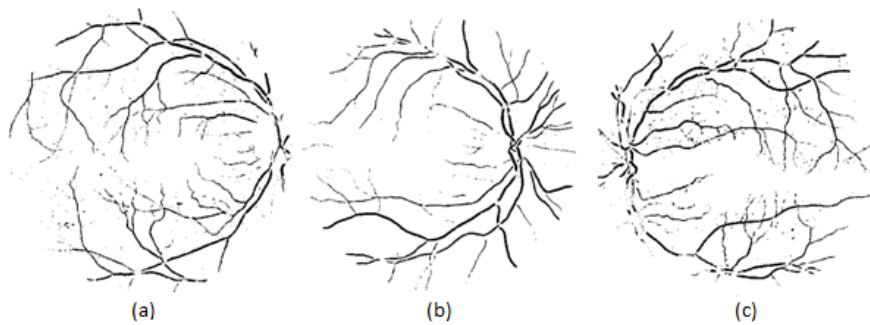
Figure 6. Binarization of enhanced image taken from sample images (a-c)

Table3. Evaluation of the proposed method by statistical performance measures.

Number of Images	AVR
Image 1	0.359
Image 2	0.7266
Image 3	0.3584
Image 4	0.3841
Image 5	0.2034
Image 6	0.3548
Image 7	0.6258
Image 8	0.6188
Image 9	455646
Image 10	0.2674
.	.
.	.
.	.
.	.
.	.
Image 44	0.3799
Image 45	0.3061
Image 46	0.2864
Image 47	0.3404
Image 48	0.5392
Image 49	0.6417
Image 50	0.495
Average	Normal -(0.62-0.735)
	Abnormal-(0.203-0.495)

[17] **Conclusion**

Early detection of hypertensive retinopathy signs is an important step in the risk stratification of hypertensive patients for medical as well as researcher's domain. Therefore, a new and easy method is developed for the enhancement and detection of blood vessels for the purpose of detection of hypertensive retinopathy. The AVR obtained by the proposed methodology for MESSIDOR dataset is 0.62-0.735 in normal cases and 0.203-0.495 in case of patients suffering from hypertensive retinopathy

In future work, automated classification of blood vessels can be introduced. Evaluations on large set of images acquired from the subjects with much wider variations of AVR can be performed to access the reliability and clinical applicability of this algorithm.

REFERENCES

[18] T.Y. Wong, P. Mitchell, *Hypertensive retinopathy*. NEJM 2004;351:2310–7.

[19] T.Y. Wong, R. Klein, B.E.K. Klein, J.M. Tielsch, L. Hubbard, and F.J. Nieto*, Retinal microvascular abnormalities and their relationship with hypertension, cardiovascular disease, and mortality*. Survey Ophthal 2001;46:59–80.

[20] K. Kumari and D. Mittal, *Drusen Quantification for Early Identification of Age Related Macular Degeneration*. Advances in Image and Video Processing, Volume 3 No 3, June (2015); pp: 28-40

[21] K. Narasimhan , V.C. Neha, K.Vijayarekha, *Hypertensive Retinopathy Diagnosis from Fundus Images by Estimation of AVR*. Procedia Engineering 12/2012; 38:980-993. DOI: 10.1016/j.proeng.2012.06.124

[22] G.C. Manikis, V. Sakkalis, X. Zabulis, P. Karamaounas, A.Triantafyllou, S. Douma, C. Zamboulis, K. Marias, *An Image Analysis Framework for the Early Assessment of Hypertensive Retinopathy Signs*. Proceedings of the 3rd International Conference on E-Health and Bioengineering - EHB 2011,24th-26thNovember, 2011, Iaşi, Romania

[23] C. Agurto, V. Joshi, S. Nemeth, P. Soliz, S. Barriga, *Detection of hypertensive retinopathy using vessel measurements and textural features*. Conf Proc IEEE Eng Med Biol Soc 2014 ; 978-1-4244-7929-0/14

[24] S. Khitran, M.U. Akram, A. Usman, U Yasin, *Automated System for the Detection of Hypertensive Retinopathy*. Image Processing Theory, Tools and Applications (IPTA), 10.1109/IPTA.2014.7001984

[25] D. Ortíz, M. Cubides, A. Suarez, M. Zequera, J. Quiroga, Dr.J.A. Gómez, Dr. N. Arroyo, *Support System for the Preventive Diagnosis of Hypertensive Retinopathy.* 978-1-4244-4124-2/10 ©2010 IEEE

[26] A.Ruggeri, E. Grisan, M.D. Luca, *An automatic system for the estimation of generalized arteriolar narrowing in retinal images*. Proceedings of the 29th Annual International Conference of the IEEE, France. 1-4244-0788-5/07

[27] V.P. Patil, P.R. Wankhede, *Pre-Processing Steps for Segmentation of Retinal Blood Vessels*. International Journal of Computer Applications (0975 – 8887) Volume 94 – No 12, May 2014

[28] K.Kumari and D.Mittal, *Automated Drusen Detection Technique for Age-Related Macular Degeneration*. Journal of Biomedical Engineering and Medical Imaging, Volume 2, No 1, Feb (2015) , pp 18-26

[29] D. Mittal , V. Kumar , S.C. Saxena , N. Khandelwal , N. Kalra*, Enhancement of the ultrasound images by modified anisotropic diffusion method*. Med Biol Eng Comput (2010) 48:1281–1291

[30] K. Sharma and D. Mittal, *Contrast Enhancement Technique for CT Images*. Journal of Biomedical Engineering and Medical Imaging, Volume 2, No 1, Feb (2015) , pp 44-50

[31] J. Kaur and D. Mittal, *Segmentation and Measurement of Exudates in Fundus Images of the Retina for Detection of Retinal Disease*. Journal of Biomedical Engineering and Medical Imaging, Volume 2, No 1, Feb (2015) , pp 27-38

[32] S.Chugh, J. Kaur, D. Mittal, *Exudates Segmentation in Retinal Fundus Images for the Detection of Diabetic Retinopathy*. International Journal of Engineering Research & Technology (IJERT) ISSN: 2278-0181 Vol. 3 Issue 10, October- 2014

[33]   Fraz, M.M., Remagnino, P., Hoppe, A., Uyyanonvara, B., Rudnicka, A.R., Owen, C.G., Barman, *Blood vessel segmentation methodologies in retinal images – A survey*. Computer methods and programs in biomedicine 108(1), 407-433 (2012).

[34] D. Mittal**,** K. Kumari, Automated detection and segmentation of drusen in retinal fundus images**.** doi:10.1016/j.compeleceng.2015.08.014

[35]   Fraz, M.M., Remagnino, P., Hoppe, A., Uyyanonvara, B., Owen, C., Rudnicka, A., Barman, *Retinal Vessel Extraction Using First-Order Derivative of Gaussian and Morphological Processing*. In: Bebis, G., Boyle, R., Parvin, B., Koracin, D., Wang, S., Kyungnam, K., Benes, B., Moreland, K., Borst, C., DiVerdi, S., Yi-Jen, C., Ming, J. (eds.)

[36]   M. Niemeijer, X. Xu, A.V. Dumitrescu, P. Gupta, B.V. Ginneken*, Automated Measurement of the Arteriolar-to-Venular Width Ratio in Digital Color Fundus Photographs*. IEEE Transactions on medical imaging, vol. 30, no. 11, November 2011

[37]   Fraz, M.M., Remagnino, P., Hoppe, A., Basit, A., Rudnicka, A.R., Owen, C.G., Barman, *Quantification of blood vessel calibre in retinal images of multi-ethnic school children using a model based approach*. Computerized Medical Imaging and Graphics 37(1), 60-72 (2013). doi:10.1016/j.compmedimag.2013.01.004

[38]   J.C. Parr, G.F.S. Spears, *General caliber of the retinal arteries expressed as the equivalent width of the central retinal artery*. Am J Ophthalmol 1974;77:472–7

[39]   J.C. Parr, G.F.S. Spears, *Mathematic relationships between the width of a retinal artery and the widths of its branches.* Am J Ophthalmol 1974;77:478–83

[40]   L.D Hubbard, *Methods for Evaluation of Retinal Microvascular Abnormalities Associated with Hypertension/Sclerosis in the Atherosclerosis Risk in Communities Study*. Ophthalmology 1999;106:2269–2280

[41]   N.M. Keith, H.P. Wagener, N.W. Barker (1939), *Some different types of essential hypertension: their course and prognosis*. Am J Med Sci, 197, 332–43

[42]   Fraz, M.M., Welikala, R.A., Rudnicka, A.R., Owen, C.G., Strachan, D.P., Barman, *QUARTZ: Quantitative Analysis of Retinal Vessel Topology and size – An automated system for quantification of retinal vessels morphology.*ExpertSystemswithApplications;42 (20),7221-7234(2015). doi: http://dx.doi.org/10.1016/j.eswa.2015.05.022

[43]   Fraz, M.M., Rudnicka, A.R., Owen, C.G., Strachan, D.P., Barman, *Automated Arteriole and Venule Recognition in Retinal Images using Ensemble Classification*. 9th International Conference on Computer Vision Theory and Applications (VISAAP), Lisbon, Portugal, 5-8 January 2014 2014

Segmentation of Liver from Abdomen CT images and 3D Visualization

[1]Ritambhara and [2]Deepti Mittal
Department of Electrical and instrumentation Engineering
Thapar University, Patiala, Punjab, India
[1]ritambhara3939@gmail.com; [2]deepti.mittal@thapar.edu

ABSTRACT

Segmentation of liver is the initial and fundamental step for the diagnosis of liver disease, 3-D volume construction and volume measurement. However, segmentation of liver is a challenging task due to it's inter and intra intensity and texture similarities among other organs present in CT abdominal images. A semiautomatic method has been proposed to segment the liver portion from CT abdominal images and their three dimensional volume construction by (i)Noise removal using median filter,(ii)Segmentation of liver portion based on active contour method using sparse field method and(iii)liver volume construction using marching cube method. Evaluation of proposed method is carried out on clinically acquired CT images and effectiveness of algorithm is evaluated by comparing manually segmented liver portion marked by radiologist with proposed method.

Keywords-Active contour, marching cube.

[44]**Introduction**

Computed Tomography (CT) is one of the imaging technique that is used to obtain cross-sectional image of soft tissues inside the body. Each cross-sectional image is termed as a "slice" of the person being imaged. These cross-sectional images are used to diagnose liver diseases and for construction of three dimensional volume of liver. There are number of imaging techniques to diagnose liver diseases like ultrasound, computed tomography and magnetic resonance imaging (MRI). Ultrasound is least expensive and most available imaging technique but it is operator dependent and does not give good quality and contrast of image based on echo genecity. Although MRI gives better contrast and is highly specific, it is very expensive and only available at specialized units. Therefore it is not as popular as CT. Computed tomography is comparatively less costly than MRI and gives better contrast than ultrasound. Therefore it is frequently applied imaging technique.

Liver is the largest organ in the body and performs many vital functions. According to American Cancer Society, liver cancer is the sixth most common cancer in the world [1]. Major cause of primary cancer is alcohol-related cirrhosis and fatty liver diseases. Fatty liver diseases are those liver diseases in which fat accumulates on the liver usually in connection with heavy use of alcohol and weight gain which increase volume of liver. Cirrhosis is end stage of liver cancer with reduced liver volume. Therefore volume measurement may be required by the radiologist to diagnose the conditions of such type of liver diseases.

Segmentation of liver is a fundamental preprocessing step for many applications such as liver tumor segmentation, 3-D (three dimensional) volume construction and volume measurement. The segmentation of liver portion is primarily done to diagnose liver tumor which is main cause of liver cancer. Another major advantage of segmentation of liver is three dimensional volume construction of liver. In three dimensional volume constructions, segmented liver slices are stacked to form a volume. 3-D volume is vitally used in tumor resection, transplantation of liver and in invasive surgery. 3-D volume construction will assist radiologist for the confirmation of liver diseases like cirrhosis and fatty liver diseases based on variation of liver volume as described above. Major challenge in 3-D modeling is determination of correspondence between segmented instances. The quality of model, completeness and accuracy are main aspects which are to be considering in modeling of 3-D volume. In this preliminary work, a method has been proposed which is designed by considering effective segmentation of liver portion from CT images. In order to develop an efficient 3-D method, an effective segmentation method is needed to be applied on the clinically acquired medical images. That's why a huge literature review has been carried out.

Ananth et al. developed a method to segment the liver in which they compare two methods Graph cut and geodesic graph cut method [2]. They achieved Dice similarity coefficient (DSC) =87.1%, processing time =1.005s in case of graph cut method and DSC =94.5%, processing time =1.009s in case of geodesic graph cut method. Main advantage of this method is to precisely localize object boundaries. Kumar et al. developed an automatic method in which they used morphological functions (erosion) in pre-processing to reduce computation time and efforts by removing extra regions and segmentation of liver is done using region growing method [3]. The main drawback of region growing method is manual seed point identification. If this seed point is not located properly, it can lead to false segmentation. Jayanthi and Kanmani developed segmentation method of region growing with morphological functions in post processing step [4]. They analyze that for entire region segmentation, region growing method has to be applied in iterative manner. Mittal and Kumari used gradient based segmentation method to find true edges in their work [5]. Lim et al. developed automatic liver segmentation method using adaptive thresholding and iterative morphological filtering [6]. They obtained an accuracy of 96%. Applied method took 2-3 minutes for total processing. A survey of different segmentation techniques are given by Rajagopal and Subbaiah [7]. They gave comparative study of region growing and thresholding based segmentation methods. They analyze that region growing methods are best employed on contrast enhanced CT images and threshold based approaches best work on the images in which intensity histogram gives neat intensity peak for input image. Massieh et al. developed a method in which they used isodata thresholding technique and Mean shift filter in preprocessing and force-driven optimized active contour (snake) to segment liver portion. It gives accuracy across 95%. This method can be further used to segment tumor portion in liver. Main limitation of the method is that snake does not stop at the boundary of liver [8]. Other limitation is that in some cases the boundary between liver and neighboring organs disappears and it becomes hard to determine the difference among different organs and this leads to erroneous segmentation. Casciaro et al. gives an adaptive initialization method to produce fully automatic processing frameworks based on graph-cut and gradient flow active contour algorithms [9]. They used mean shift filter for pre-processing because mean shift filter preserve edges and does not blur edges. In their study graph-cut algorithm and active contour gradient vector flow gives DSC =95.49% and 96.17% respectively. In above defined method preprocessing step consumes 70% of total processing time.

Massoptier and Casciaro developed a method in which they used mean shift filter in preprocessing step in which designed filter reduce pre-processing time by 90% and were combined to an active contour technique using gradient vector flow in order to obtain smoother segmentation [10]. A 3-D stastical model was constructed to best define the shape of liver. Elaziz et al. developed a method based on region-growing [11]. They claim that their algorithm decreases the computation time by removing the regions of other structures as most techniques in use today are very time consuming. A lot of work has been done on CT images [12][13].

Brief literature review of recent development is shown in Table1. In literature review, authors states that mean shift filter consume most of the processing time therefore a method is designed in which median filter is used. It leads comparatively less time with not much deterioration in segmented result. It will be further helpful in real time implementation of the proposed method.

Table1.Summary of previous research work related to segmentation of liver and construction of 3D volume

Method	Year	Dataset (CTimage)	Image processing technique (preprocessing)	Image processing technique (segmentation)	Parameter	Pros	Cons
Lim *et al.* [6]	2005	-	Thresholding based	Contour method based on morphological filtering	AC =96%	Preprocessing steps are more. Processing time 20-60s/slice.	Total processing time is 2-3 minutes.
Massoptier and Casciaro [10]	2008	21	Mean shift filter based	Active contour using gradient vector flow	VO=94.2% Ac=3.7mm	GVF active contour converge faster than active contour.	Designed filter save 90% of processing time.
Campadelli *et al.*[14]	2009	100	Images resized to 256×256 pixels, 3×3 median filter based.	Gray level based framework	SVO=94%	Down sampling factor reduce computation cost.	-
Moghe *et al.* [15]	2011	58	No preprocessing	Automatic thresholding	-	If Intensity variation is sharp.	-
Massieh *et al.* [8]	2011	15	Isodata thresholding and Mean shift filter based	Force-driven optimized active contour (snake**)**	Se=95% Sp=99%	Method can be used further for diagnosing the lesions.	Snake does not stop at the Boundary of liver.
Casciaro *et al.* [9]	2012	10	Mean shift filter	Graph-cut algorithms	DSC=96.2%	High accuracy	Filtering consume 70% of process time.
Ananth *et al.* [2]	2014	-	Mean shift filter	Geodesic Graph cut method.	DSC=94.5% PT=1.009s	Geodesic graph cut is better	-

*AC=average correctness, VO=volume overlap, DSC= Dice similarity coefficient, PT=processing time, Se=sensitivity, Sp=specificity, SVO= Symmetric volume overlap, Ac= Accuracy

[45]**Materials and methods**

The proposed method is applied on a data set containing 75 CT images. CT images are of 514×514 dimensions. The data set of CT images is collected from the MAX hospital, Delhi, India. The method is implemented in MATLAB version 8.The block diagram representation of the proposed is shown in Fig.1,

where it is expressed in terms of three major steps such as: preprocessing, segmentation of liver portion using active contour method and 3D volume construction.
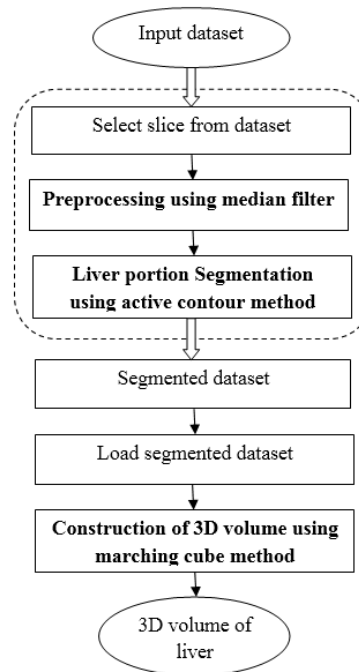
Figure 1 Block diagram representation of proposed methodology for 3D volume construction

a. Preprocessing

CT images may be noisy because of its making procedure, data acquisition and construction of image from the acquired data. Also, near boundary portion of the CT images contain patient related information along with other information. Therefore it is ethically necessary to hide that information in each CT image. Therefore cropping is applied as initial step of preprocessing and after that median filter is applied for the removal of noise dataset. Applied method uses resized CT image slices in which slices of 514x514 dimensions are reduced to 307x457 dimensions. This step removes all text information which is not necessary for processing and reduces processing time.

Median filter of size 3x3 is convolved with CT image. The noise removal in an image is necessary for effective segmentation; at the same time it is important to preserve the edges. Edges in CT image are of critical importance for the visual appearance of images. The median filter is demonstrably better than Gaussian blur for removing noise whilst preserving edges for a given, fixed window size for moderate level noise (Gaussian).

b. Liver segmentation using Active contour method

In this work, active contour method is used to segment liver portion from the clinically acquired abdominal CT images. Active contour method finds the curve that best separates objects in an image [16]. Active contour or snakes is an energy minimizing spline guided by external constraint forces and pulled by image forces toward features like edge detection, subjective contours, motion tracking etc. Snakes falls into local energy minima for which they rely on other mechanisms to place them near the desired contour. Snakes

will try to match a deformable model to an image by means of energy minimization. Total energy of snakes is given by

$$E_{snakes} = \int_0^1 (E_{int}(b(x)) + E_{im}(b(x)) + E_{con}(b(x)))dx$$

E_{int} = Internal energy due to bending(elasticity)

E_{im} = Image forces pushing the snake toward image features

E_{con} = External constraints put the snakes near the desired local minima

Internal energy of snake is composed of two parameters elasticity and rigidity which can be expressed by

$$E_{int} = \int_l (\frac{1}{2}\alpha(x)|b(x)|^2 + \frac{1}{2}\beta(x)|b(x)|^2))dx$$

$\alpha(x), \beta(x)$ control the amount of stretch in the snake and the amount of curvature in the snake respectively. Image energy is a function of features of the image. I(x,y) image is a combination of lines, edges and termination. These can be expressed as

$$E_{image} = w_{line}E_{line} + w_{edge}E_{edge} + w_{term}E_{term}$$

Here $w_{line}, w_{edge}, w_{term}$ are weights of features, higher values of feature will indicate higher contribution of that salient feature.

Line functional is the intensity of image and is given by

$$E_{line} = I(x, y)$$

Edge functional will attract the snake to large intensity gradient

$$E_{edge} = -|\nabla I(x, y)|^2$$

Termination functional will attract the snake towards termination of line segment or corner. Constraint energy will guide the snake to go away or towards a particular feature. Proposed method given by Kass *et al.*[17] has various limitations therefore many researchers had improved the active contour method by introducing various models based on edge and region functional. One such model is geometric or geodesic snake model based on Euclidian curve shortening evolution. These models are implemented using level sets. Level sets have a limitation of slow computation. This limitation is overcome by sparse field method (SFM) introduced by R.Whitaker [18]. Sparse field method drastically reduces computation times for level set methods. The initial contour is chosen to include the object. The sparse field method uses lists of points that are composed of zero level set as well as neighboring points to the zero level set. A very efficient representation of contour is done by using these lists and carefully moving points to and from the appropriate list. To minimize some segmentation energy level sets are deformed. There are many such active contour energies. Most popular is Chan-Vese energy [19]

$$E = \int_{interior} (I - \mu)^2 + \int_{exterior} (I - \mu)^2$$

In SFM the speed of curve updates is dependent only on the length of the curve, and not on the size of the image. The active contour will stop its iterations when recent five iterations give the same result.

c. Three Dimensional Volume Construction

The final step in proposed methodology is 3-D volume construction from 2-D images. That will be primarily used for visualization and quantization of liver. Volume construction of CT images will reduce inter observer variability by correctly evaluating the size of liver which is irregular in shape and size. Various methods have been introduced to construct stastical shape models or 3-D volume [20]. Heimann et al. had given a detailed review of all the stastical shape models based upon alignment, correspondence, registration etc. In this paper marching cube method is used to display overall volume of CT 2-D images. One such efficient method for volume construction is Marching cube method. It was introduced by Lorensen and Cline in 1987 [21].

Marching cubes algorithm proceeds through the voxles or scalar field. It takes eight neighbor locations at a time. Therefore these points form an imaginary cube. Then polygon(s) is determined which will be used to represent the part of the isosurface that will pass through this cube. The individual polygons are then combined to form a desired three dimensional surface. This whole process is done by creating an index, since there are eight vertices of cube and two neighbor slices; therefore there are total 256 configurations within the cube. If value of one of the vertices in the cube is higher than the iso-value that means that point is inside the surface therefore that particular bit is set to one. Otherwise if value of vertices is lower than iso-value, it is set to zero. Finally generated polygons are placed at appropriate location by linear interpolation. In this way 3-D volume surface is acquired using Marching cube method.

[46]**Experimental results and discussion**

The proposed methodology is evaluated visually and quantitatively, analysis is done on CT images. In the first step of the method segmentation of liver is carried out on the acquired CT images using active contour method. These results of segmentation are demonstrated in fig. 2 on an example image.
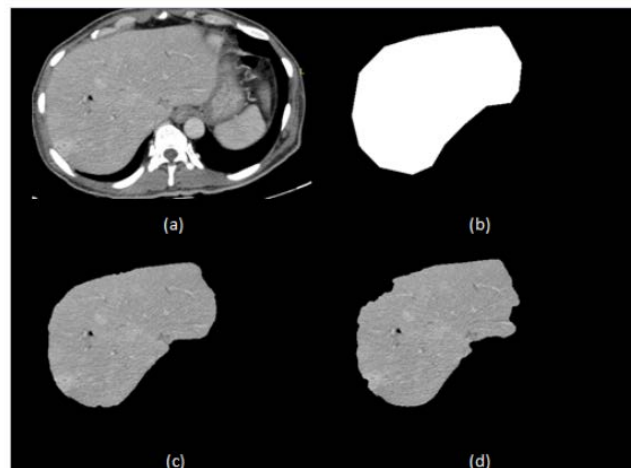
Figure 2 Liver portion segmentation result (a) 307x457 resized Original image (b) Initial mask (c) Segmented image with 50 iterations (d) Segmented image with 200 iterations

Figure 2(a) is a resized image of dimension 307x457. Noise in clinically acquired CT image is removed using median filter and it will take less time for preprocessing. Active contour method was applied to segment liver region. Fig.2 (b) is a mask obtained by initializing points on CT image by prior knowledge of position and shape of liver. The points should be marked at the boundary of liver region for accurate segmentation. Active contour method uses 'Chan-vese'or 'edge' method to minimize its segmentation energy and to

extract edge features from the image. 'Chan-vese' cannot correctly distinguish the edges when the intensity variation is not so sharp. Therefore 'edge' functional is used to detect the edges in CT images. Segmentation method will stop iterate when previous five iterations give same result. Fig.2(c) shows segmentation result with maximum 50 iterations. 'Edge' method has a natural tendency to shrink at the boundary of the region with increase in number of iterations. During segmentation it is essential to initialize the points outside the boundary of region of interest. Therefore a threshold is essential to set, otherwise image will get deteriorate. Fig 2(d) shows segmented CT image after 200 iterations. From fig. 2(d) the need of thresholding can be easily visualized where image got deteriorate at the boundary of liver portion due to increase in number of iterations.
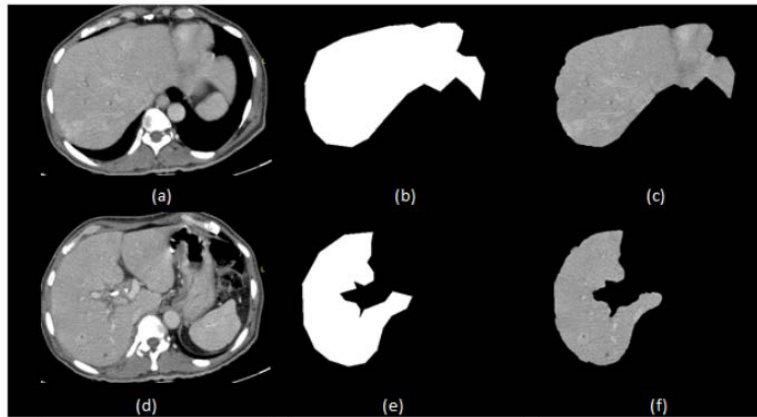
Figure 3 from top to bottom: CT images with different difficulty cases in CT dataset.

Figure 3 shows the segmentation results on different samples of CT images where difficulty level is comparatively high. From top to bottom in Fig.3 it is clearly visualized that active contour method can efficiently segment liver portion from CT images. Quantative analysis of active contour method is carried out by shape feature extraction. Table 2 shows the result of shape feature extraction. *Area* tells us about the actual number of pixel in segmented region. *Perimeter* is the total distance around the boundary of 2D slice. *Equiv-diameter* gives diameter of region of interest. Table 2 shows the result of clinically acquired manually segmented liver CT images by radiologist. Table 2 shows the result of active contour method applied on CT images. Relative accuracy is calculated by subtraction of manually segmented result by radiologist and active contour method divided by manually segmented result.

$$\text{Relative accuracy} = \frac{\text{manually segmented result by radiologist} - \text{active contour method result}}{\text{manually segmented result by radiologist}}$$

Comparative performance analysis shows the comparison of results of manually segmented CT images by radiologist and segmented liver portion results using active contour method in Table2. In this preliminary work on 2-D images, 3-D volume is constructed using marching cube method. In first step, segmented liver dataset is loaded. Fig.4 is showing whole process of construction of 3-D volume. 3-D volume will give a better visualization of all CT image slices

Table2: Comparison between manually segmented image result and active contour method result

CT images	Area (pixels)			Perimeter			Equiv-diameter		
	Manually segmented liver portion	Segmented liver portion by proposed method	Relative accuracy	Manually segmented liver portion	Segmented liver portion by proposed method	Relative accuracy	Manually segmented liver portion	Segmented liver portion by proposed method	Relative accuracy
Slice 1	45982	43724	0.0491	875.09	823.08	0.0591	241.88	235.847	0.0249
Slice 2	45926	43155	0.0603	901.62	867.56	0.0377	241.73	234.306	0.0177
Slice 3	46777	44320	0.0525	874.59	838.16	0.0416	243.96	237.450	0.0266
Slice 4	46274	45120	0.0249	882.60	850.53	0.0363	242.64	239.580	0.0129
Slice 5	42608	43981	0.0322	1248.60	860.90	0.3105	232.79	236.540	0.1608
Slice 6	40217	37583	0.0654	884.11	1223.70	0.3830	226.15	218.590	0.0334
Slice 7	29019	27385	0.0560	960.98	929.81	0.0324	192.09	186.570	0.0287
Slice 8	28716	26492	0.0774	1026.00	954.94	0.0694	191.09	183.500	0.0397
Slice 9	28523	26095	0.0851	981.07	956.49	0.0250	190.44	182.124	0.0461
Slice 10	26712	25840	0.0321	1007.60	943.16	0.0639	184.27	181.244	0.0164
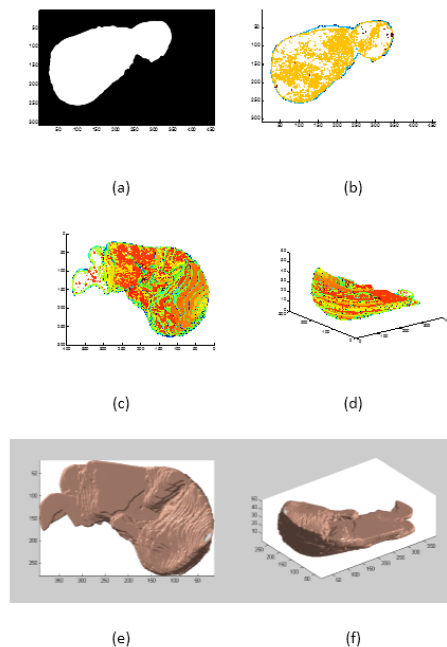
Figure 4. 3D volume construction steps: (a) 2D slice from CT dataset (b) contour slice (c) 3D contour slices stacked from 1 to 51 and its volume at 45 degree rotation (d) 3D volume of 51 slices at 90 degree rotation.

From fig. 4 it can be clearly visualized that using marching cube method 3-D volume can be constructed. Fig.4 (a) shows one of 2-D slice from dataset. Fig. 4(b) shows 2-D contour of slice.fig 4(c) is the 3-D visualization of various slices stacked together .fig 4(d) is the smoothed 3-D model of liver.

[47]**Conclusion and future scope**

A methodology is designed in the proposed work to construct 3-D volume of the liver using abdominal CT images. The methodology can be described in three main steps: (i) Noise removal (ii) segmentation of liver potion from abdominal CT images (iii) 3-D volume construction. The removal of noise from CT images is

carried out by median filtering because of its simplicity and computational time than other filtering techniques. Segmentation of liver portion from CT images is carried out using active contour method and 3-D volume construction is done using marching cube method.

In future work this semiautomatic method can be improved by making it fully automatic to avoid user interaction. Furthermore, 3-D model that is constructed by using segmented 2-D images has certain irregularities and is not smooth. Therefore the future research work can be focused on the improvement of smoothness of model and its parameterization.

REFERENCES

[1] Corporate Center: American Cancer Society Inc. 250 Williams Street, NW, Atlanta, GA 30303-1002 (404) 320-3333.

[2] C. Ananth, D.L.R. Bai , K. Renuka, C. Savithra, A. Vidhya, Interactive Automatic Hepatic Tumor CT Image Segmentation, International Journal of Emerging Research in Management &Technology ISSN: 2278-9359 (Volume-3, Issue-1),2014.

[3] S.S. Kumar, R.S. Moni, J. Rajeesh, Automatic Segmentation of Liver and Tumor for CAD of Liver, Journal of advances in information technology, vol. 2, no. 1, February 2011.

[4] M. Jayanthi and B. Kanmani, Extracting the Liver and Tumor from Abdominal CT Images, 2014 Fifth International Conference on Signals and Image Processing 978-0-7695-5100-5/13 $31.00 © 2013 IEEE.

[5] D. Mittal and K. Kumari, Automated detection and segmentation of drusen in retina fundus images, Computers and Electrical Engineering 47 (2015) 82–95.

[6] S.-J. Lim, Y.-Y. Jeong, Y.-S. Ho, Automatic liver segmentation for volume measurement in CT images, 1047-3203/$-see front matter 2005 Elsevier Inc.

[7] R. Rajagopal and P. Subbaiah, A survey on liver tumor detection and segmentation methods, ARPN Journal of Engineering and Applied Sciences Vol. 10, NO. 6, April 2015.

[8] N.H. Abdel-massieh, M.M. Hadhoud, and K.A. Moustafa, A fully automatic and efficient technique for liver segmentation from abdominal CT images, presented at Informatics and Systems (INFOS), 2010 The 7th International Conference on, 2010.

[9] S. Casciaro, R. Franchini, L. Massoptier, E. Casciaro, F. Conversano,A. Malvasi and A. Lay-Ekuakille, Fully Automatic Segmentations of Liver and Hepatic Tumors From 3-D Computed Tomography Abdominal Images: Comparative Evaluation of Two Automatic Methods, IEEE Sensors journal, vol. 12, no. 3, March 2012.

[10] L. Massoptier, S. Casciaro, A new fully automatic and robust algorithm for fast segmentation of liver tissue and tumors from CT scans, Euro Radial (2008).

[11] O.F. Abd-Elaziz, M.S. Sayed and M.I. Abdullah, Liver Tumors Segmentation from Abdominal CT Images using Region Growing and Morphological Processing, 978-1-4799-5807-8/14/$31.00 @2014 IEEE.

[12] K. Sharma and D. Mittal, Contrast Enhancement Technique for CT Images, Journal of Biomedical Engineering and Medical Imaging, Volume 2, No 1, Feb (2015) , pp 44-50.

[13] A. Krishan, D. Mittal, International Journal on Recent Technologies in Mechanical and Electrical Engineering (IJRMEE), Volume: 2 Issue: 5, May 2015.

[14] P. Campadelli, E. Casiraghi, S. Pratissoli and G. Lombardi, Automatic Abdominal Organ Segmentation from CT images, Electronic Letters on Computer Vision and Image Analysis 8(1):1-14, 2009.

[15] A.A. Moghe, J. Singhai, S.C Shrivastava, Automatic Threshold based Liver Lesion Segmentation in Abdominal 2D-CT Images, International Journal of Image Processing (IJIP), Volume (5): Issue (2): 2011.

[16] V. Caselles, R. Kimmel, G. Sapiro, Geodesic active contours, International Journal of Computer Vision, Volume 22, Issue 1, pp. 61-79, 1997.

[17] M. Kass, Witkin and Terzopolous, Snakes: Active contour models, International Journal of Computer Vision, pages 321-331, 1987.

[18] R. T. Whitaker, A level-set approach to 3D reconstruction from range data, International Journal of Computer Vision, Volume 29, Issue 3, pp.203-231, 1998.

[19] T.F. Chan and L.A. Vese, Active contours without edge, IEEE Transactions on Image Processing, Volume 10, Issue 2, pp. 266-277, 2001.

[20] T. Heimann and H.P. Meinzer, Statistical shape models for 3D medical image segmentation: A review, Medical Image Analysis 13 (2009) 543–563, 1361-8415/$.

[21] W. E. Lorensen and H.E. Cline, Marching cubes: A high resolution 3D surface construction algorithm, Computer Graphics, Volume 21, Number 4, July 1987.

Classification of EEG Signals Produced by RGB Colour Stimuli

[1]Saim Rasheed and [2]Daniele Marini

[1]Department of Information Technology, Faculty of Computing and IT
King Abdulaziz University, KSA
[2]Dipartimento di Informatica, Università degli Studi di Milano, Italia
srahmed@kau.edu.sa

ABSTRACT

In this paper we have presented results for classification of electroencephalograph (EEG) signals produced by the random visual exposure of primary colours i.e. red, green and blue to the subject while sitting in a dark room. Event-related spectral perturbations (ERSP) are used as features for support vector machine (SVM). Our objective was to classify the EEG signals as Red, Green and Blue classes and we have successfully classified the three visual conditions having accuracy of 84%, 89% and 98% with linear, polynomial and radial basis function kernels respectively with in all the groups of data among all the subjects.

[48]Introduction

In virtual and physical environment, a person can control the devices such as movement of cursor on monitor screen and controlling wheel chair using EEG-based non-invasive Brain-Computer interface (BCI) applications (Pires et al. 2008; Leeb et al. 2006). The electrical activity produced by the brain is recorded using electrodes placed over the scalp. The experiments are usually designed to record EEG signals as P300, or mu rhythm based event-related potentials or ERP that can more precisely describe the dynamics of brain related activities. For instance, BCI users concentrate on imagination of hand or foot movement (Pfurtscheller & Neuper 2001) or fixate their gaze on monitor screen to interact with Speller applications (Farwell & Donchin 1988). These mental activities are selected in such a way to activate the related brain area and may vary widely across different experiments, subjects and the related application. Such BCI systems performances may be improved with the help of feedback. In (Wolpaw et al. 2002), Wolpaw et al has presented an overall generic review of brain-computer interface systems that provide comprehensive detail on fundamental studies. The most meaningful information exist in the frequency bands, delta ($0.1 - 4$ Hz), theta ($4 - 8$ Hz), alpha ($8 - 12$ Hz) and beta ($12 - 30$ Hz). These are most commonly known frequency bands and depend on researcher's purpose for the analysis of a particular band to be utilized in a certain case. Usually, EEG signals recorded from scalp are very weak and may vary in the range from 5 to 100 microvolts during recording and amplified later for further signal processing. During recording of EEG signals, noise such as main's electrical impulse and other artifacts like EOG/EMG signals may interfere. Although, the subjects are instructed to avoid eye blinking and/or muscle movement, even then the signals are processed to eliminate such information using mathematical algorithms e.g. Independent component analysis (ICA) (Hallez et al. 2009; Jung et al. 2000) and principal component analysis (PCA) (Foresta et al. 2009) before performing classification task.

The ultimate task of any BCI system is the classification of EEG signals (Chiappa & Barber 2006; Guan & Chen 2008; Lotte et al. 2007; Benjamin et al. 2002; Krusienski et al. 2008) which reflects the growing interest of researchers in EEG-based BCI and present published results doing analysis, evaluation and assessment of classification algorithms. For BCI applications, it is necessary to implement online classification in order to see real time execution which is a challenging task for signal processing and machine learning experts. However, an earlier offline analysis of EEG signals helps us in improving our classification accuracies. Once the brain signal is classified, it is fed to the outer world application to perform the desired operation. In this paper, we have performed an experiment and presented the results for offline classification of EEG signals recorded from the scalp, produced by primary colours stimuli, red, green and blue, presented at random. The purpose of the experiment is to verify, if either the observation of different real colours or their corresponding imagination of colours can be detected in the selected EEG frequency combination, and to select best frequency combination to maximize differences through colour signals in order to find a Way-In to further establish our argument and to provide a baseline to be compared with more complex visual stimuli to evaluate the effects of colours to navigate in an immersive VR environment for developing future BCI applications (Leeb et al. 2006). For example, we can develop a virtual reality (VR) application to navigate into VR environment. In a first and preliminary version, developed application will exhibit the traffic light signals. A moving vehicle may be stopped when turning ON the Red light, upon recognition of red colour through EEG signals. Similarly, upon recognition of the green light, a stopped vehicle will start moving. We suggest this procedure may be a faster and more effective communication channel than those based on motor imagery described in [2]. This way, we may use colours as controllable parameter in VR environments. Another application of such colour recognition system could be for colour blind and/or blind people (Dobelle 2000). These applications are quite novel in their fields and needs extensive collaborative research work in different domains.

[49] **Experimental Design**

Concerning the experimental settings, seven male subjects have undertaken the experiment, age ranging from 20 to 36 years. All subjects were free of neurological and psychiatric disorders and have normal colour vision. Experiment was performed in a dark room in front of a large curved screen on which the colour was presented as a square with size of 10 degree angle on a much wider gray background. The subjects were seated on a comfortable chair. Distance between the subjects and the screen was 3.5 meters and 1.5 meters high from the ground. The luminosity of each colour was kept constant at 4.5 cd/m2 and measured using the device Minolta SPOTMETER F. Screw-able gold EEG electrodes were used on the subject's scalp at P3, P4, O1 and O2 sites and referenced to right ear lobe and grounded at site AFz as shown in figure 1.

Figure 1. Electrode placement layout.

Experiment protocol is shown in figure 2 that depicts the duration of one sequence. In this protocol, each colour was presented for three seconds, twice in one sequence and the subject was instructed to imagine the same colour for three seconds in the same sequence twice. There are eight events in one sequence. Only one colour is presented in one sequence. After all the events are occurred in a sequence then the next sequence is started and another colour is presented. Uniform gray background colour was displayed before and after every target colour to balance possible after-effects of the RGB stimuli (Yoto et al. 2007). All impedances were kept below 5kΩ. EEG signals were recorded using BCI2000 (Schalk et al. 2004) with g.tec's g.MOBIlab+ portable device sampled at 256 Hz, processed and analyzed offline using EEGLAB (Delorme & Makeig 2004) that runs with MATLAB. Signals were band pass filtered from 0.1 Hz to 30 Hz. Each colour was presented 60 times randomly, resulting in 60 trials of each colour from each subject. Each trial contains 768 data points after the onset of stimulus. Once, all the EEG signals were recorded they were brought into EEGLAB for offline processing and analysis. EEGLAB has a vast compatibility to import EEG signals into MATLAB's workspace which are recorded with different devices using BCI2000. Epochs were extracted from continuous data for each colour. Each epoch lasts for three seconds i.e. one second before the event occurred and two seconds afterwards. To reduce the effects of abnormal values, those trials for which EEG signals crossed ± 60 µV were rejected and some segments were also dropped by visual inspection that did not cross ± 60 µV but were unreliable in further computations. Some trials were dropped due to artifacts like EOG/EMG signals, from each colour for each subject.

Figure 2. Experiment protocol

a. Artifact Rejection

ICA is a method that provides us the capability to solve the problem of Blind Source Separation. It can identify N independent source signals, $S = \{s_1(x), s_2(x), \cdots s_N(x)\}$ (e.g. different voices, music or other sound sources) from N linear mixtures matrix $M = \{m_1(x), m_2(x), \cdots m_N(x)\}$, that can be modeled by multiplying the source matrix S by an unknown square matrix T such that

$$M = TS \tag{1}$$

In order to discriminate the source signals from mixtures, it is assumed that sources s_i are independent and their mixtures are not. Having no prior knowledge of source signals or about the process, how the signals were mixed, the objective is to approximate another matrix $U = \{u_1(x), u_2(x), \cdots u_N(x)\}$, identical to source signals by specifying the filter to linearly invert the mixing process such that

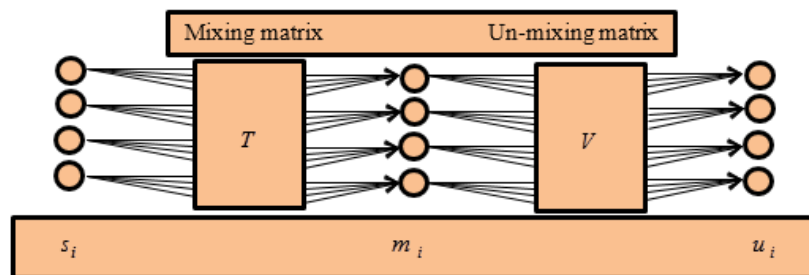$$U = VM \tag{2}$$

where V is a square matrix.

Figure 3. The general process of ICA.

In our case, we have four electrodes that measure the four mixtures of signals. Applying ICA decomposes the mixtures into four independent source signals. The general overview of process of ICA is shown in figure 3. Electrode measurements m_i are assumed to be composed of a linear mixture of independent sources s_i . Un-mixing matrix V is produced using ICA, which decompose m_i to estimate the independent sources u_i . After identification of components, the one that contains EOG/EMG artifacts is subtracted and artifact free EEG is obtained for further feature extraction and classification. Software routines are available within EEGLAB for detection of artifacts based on ICA, however marking and rejection of artifacts is done manually before feature extraction and classification tasks. A detailed review on theory of ICA and their practical use is discussed in (Jung et al. 2000; James & Hesse 2005; Jung et al. 2000; Stone 2004).

b. Event-Related Spectral Perturbation as Features

ERSP is a measure to study the event-related brain dynamics. It reflects the information about variation in power at different frequencies at a certain time point. Makeig in (Makeig 1993) reported that according to several studies, event-related potentials (ERPs) are not capable of capturing maximum brain's response to events due to their instability and not being fully independent of EEG. Due to this limitation of ERPs being used as features may not classify satisfactorily, which we also tried to use in our classifier but attained less accurate results. On the other hand, we have used event-related spectral perturbation (ERSP) (Makeig et al. 2004; Makeig 1993; Huang et al. 2005) values in terms of time-frequency measurements as features for the classifier and the results are dramatically improved. "*To compute an ERSP, baseline spectra are calculated from the EEG immediately preceding each event. The epoch is divided into brief, overlapping data windows, and a moving average of the amplitude spectra of these is created. Each of these spectral transforms of individual response epochs are then normalized by dividing by their respective*

mean baseline spectra. Normalized response transforms for many trials are then averaged to produce an average ERSP" (Makeig 1993) .

c. Support Vector Machine as Classifier

We have used SVM as classifier because it has been proved to be very good in classification tasks (Kaper et al. 2004; Rakotomamonjy et al. 2005; Garrett et al. 2003; Benjamin et al. 2002; Peterson et al. 2005). SVM constructs a hyperplane in the simplest case that is used for classification to separate the data points belonging to two different classes. This hyperplane is chosen in such a way to maximize the distance margin δ , as shown in figure 4 and 5, to the closest training data points of any class. In general, the larger the margin is, the higher is the classification accuracy. SVM may broadly be categorized as hard margin and soft margin (Abe 2005). However, the SVM theory was developed by Vapnik (Vapnik 2000) and a good review on classification algorithms for BCI research is presented in (Lotte et al. 2007). To classify M, $m-$ dimensional training data points x_i ($i=1,\cdots,M$) which either belong to class 1 or class 2 and the associated labels be $y_i=1$ for class 1 or $y_i=-1$ for class 2. A decision function is defined as $F(x)=w^T x+b$, where w is an $m-$ dimensional vector and b is the bias term. If the data is linearly separable then no data points will satisfy

$$w^T x + b = 0 \tag{3}$$

So, for $i=1,\cdots,M$

$$w^T x_i + b \begin{cases} \geq 1 \\ \leq -1 \end{cases} \text{for} \quad \begin{matrix} y_i = 1 \\ y_i = -1 \end{matrix} \tag{4}$$

Equation (4) may be written as

$$y_i(w^T x_i + b) \geq 1 \text{ for } i=1,\cdots,M . \tag{5}$$

The function,

$$F(x)=w^T x + b = c \text{ for } -1 < c < 1 \tag{6}$$

defines the hyperplane that separates the data points x_i ($i=1,\cdots,M$). For $c=0$, the separating hyperplane lies in the middle of two hyperplanes with $c=1$ and -1. Pictorial representation of SVM in case of two class problem for hard margin is shown in figure 4. The optimal separating hyperplane can be obtained by solving the optimization problem,

Minimize,

$$Z(w)=\frac{1}{2}\|w\|^2 \tag{7}$$

subject to the constraints,

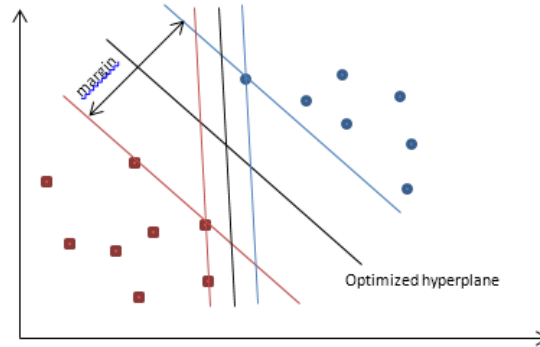$$y_i(w^T x_i + b) \geq 1 \text{ for } i=1,\cdots,M \tag{8}$$

Figure 4. A separating hyperplane in two class problem for hard margin case.

Equation (7) forms a quadratic optimization problem with inequality constraints expressed by (8). This constrained optimization problem can be solved by solving its equivalent unconstrained problem using the saddle points of the Lagrangian functional,

$$Z(w,b,\alpha) = \frac{1}{2} w^T w - \sum_{i=1}^{M} \alpha_i \left[y_i (w^T x_i + b) - 1 \right] \qquad (9)$$

Where $\alpha = (\alpha_1, \cdots, \alpha_M)^T$ and α_i are the non-negative Lagrange multipliers. Lagrangian must be minimized with respect to w and b and needs to be maximized w.r.t $\alpha_i \geq 0$. This problem can be solved into its primal space of parameters w and b and also in dual space of lagrange multipliers α_i. The approach of dual space gives us insightful results as it has the number of variable as the number of training data. Equation (9) is manipulated with Karush-Kuhn-Tucker (KKT) conditions (Abe 2005) to get the dual pro

Maximize,

$$Z(\alpha) = \sum_{i=1}^{M} \alpha_i - \frac{1}{2} \sum_{i,j=1}^{M} \alpha_i \alpha_j y_i y_j x_i^T x_j \qquad (10)$$

with respect to α_i subject to the constraints

$$\sum_{i=1}^{M} y_i \alpha_i = 0 \text{ and } \alpha_i \geq o \qquad \text{for } i = 1, \cdots, M \qquad (11)$$

which is a hard margin SVM. Using lagrangian functional in (9) with KKT conditions we obtain

$$w = \sum_{i=1}^{M} \alpha_i y_i x_i \qquad (12)$$

and

$$\sum_{i=1}^{M} \alpha_i y_i = 0 \qquad (13)$$

to finally get the decision function as

$$F(x) = \sum_{i \in S} \alpha_i y_i x_i^T x + b \qquad (14)$$

where S is the set of support vector indices along with

$$b = \frac{1}{|S|}\sum_{i \in S}\left(y_i - w^T x_i\right) \tag{15}$$

Hence the unknown datum x belongs to either class 1 if $F(x) > 0$, or class 2 if $F(x) < 0$ and remains unclassifiable if $F(x) = 0$.

Now SVM introduces slack variables $\xi_i \geq 0$ in case of soft margins and the optimization problem turned into minimizing

$$Z(w,b,\xi) = \frac{1}{2}\|w\|^2 + C\sum_{i=1}^{M}\xi_i^l \tag{16}$$

subject to the constraints

$$y_i(w^T x_i + b) \geq 1 - \xi_i \quad \text{for } i = 1, \cdots, M. \tag{17}$$

Where $\xi = (\xi_1, \cdots, \xi_M)^T$ and C is the margin parameter that determines the trade-off between the maximization of the margin and minimization of the classification error. The values for l are either 1 or 2 calling SVM either L1 soft margin SVM (L1SVM) or L2 soft margin SVM (L2SVM) respectively. Pictorial representation of SVM in case of two class problem for soft margin is shown in figure 5. Considering L1SVM, Lagrangian multipliers α_i and β_i are introduced likewise linearly separable case and we get,

$$Z(w,b,\xi,\alpha,\beta) = \frac{1}{2}\|w\|^2 + C\sum_{i=1}^{M}\xi_i - \sum_{i=1}^{M}\alpha_i(y_i(w^T x_i + b) - 1 + \xi_i) - \sum_{i=1}^{M}\beta_i\xi_i \tag{18}$$

where $\alpha = (\alpha_1, \cdots, \alpha_M)^T$ and $\beta = (\beta_1, \cdots, \beta_M)^T$ with $\alpha_i + \beta_i = C$.
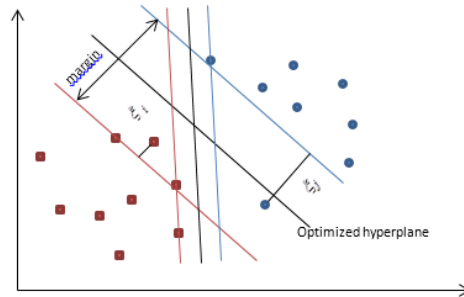

Figure 5. A separating hyperplane in two class problem for soft margin case.

The Dual problem for L1SVm is the same as dual problem for hard margin SVM described in (10) and (11). The only difference is that α_i cannot exceed C i.e. causing an extension in one of the constraints in (11) is $C \geq \alpha_i \geq 0$ for $i = 1, \cdots, M$. For three class or multiclass problem, readers may see (Steinwart & Christmann 2008; Abe 2005) for details.

If the data is not linearly separable then we can define a function that map the original input lower dimensional data into higher dimensional feature space also called dot-product space in order to enhance the linear separability. Such functions that perform mapping from lower to higher dimensional feature space are called Kernels which give us the advantage of not treating the higher dimensional feature space explicitly. This approach is also known as *kernel trick*. Given that the non-linear vector function

$$q(x) = (q_1(x), \cdots, q_n(x))^T \tag{19}$$

maps the $m-$ dimensional input vector x into the $n-$ dimensional feature space and the linear decision function in the feature space is defined as

$$F(x) = w^T q(x) + b \tag{20}$$

where w is an $n-$ dimensional vector and b is a bias term. Hilbert-Schmidt theory says that if a function $K(x,x')$ is symmetric and satisfies

$$\sum_{i,j=1}^{M} k_i k_j K(x_i, x_j) \geq 0 \tag{21}$$

then there exists a function $q(x)$ that maps x into the dot product feature space and satisfies

$$K(x,x') = q^T(x)q(x') \tag{22}$$

This $K(x,x')$ is used in training and classification instead of $q(x)$. The dual problem in the feature space using kernel is as follows

Maximize,

$$Z(\alpha) = \sum_{i=1}^{M} \alpha_i - \frac{1}{2} \sum_{i,j=1}^{M} \alpha_i \alpha_j y_i y_j K(x_i, x_j) \tag{23}$$

subject to the constraints

$$\sum_{i=1}^{M} y_i \alpha_i = 0, \quad C \geq \alpha_i \geq 0 \quad \text{for } i = 1, \cdots, M \tag{24}$$

The decision function that contain kernel expression becomes

$$F(x) = \sum_{i \in S} \alpha_i y_i K(x_i, x) + b \tag{25}$$

where b is given by

$$b = \frac{1}{U} \sum_{j \in U} (y_j - \sum_{i \in S} \alpha_i y_i K(x_i, x_j)) \tag{26}$$

Here U is the set of unbounded support vector indices.

Generally used kernels in SVM are linear kernel, polynomial kernel and Radial Basis Function (RBF) kernel. However, three-Layer Neural Network Kernels and some other kernels are briefly discussed in (Abe 2005; Wang 2005). Most commonly used kernel in BCI community is RBF or Gaussian kernel. The mathematical expression for linear, polynomial of degree d and RBF kernels are given in (27), (28) and (29) respectively.

$$K(x,x') = x^T x' \tag{27}$$

$$K(x,x') = (x^T x' + 1)^d \tag{28}$$

$$K(x,x') = \exp(-\gamma \|x - x'\|^2) \tag{29}$$

Here γ is a parameter for controlling the radius.

SVM that uses RBF kernel is known as Gaussian SVM or RBF-SVM. RBF converts the data space to higher dimensional feature space making separation much more likely for nonlinear cases. An SVM with linear

kernel, called linear SVM is also used widely. Linear SVM (Rakotomamonjy et al. 2005; Garrett et al. 2003; Benjamin et al. 2002) and RBF-SVM (Kaper et al. 2004; Garrett et al. 2003), both have been applied to BCI research quite successfully.

[50]**Results and Discussion**

Here we have presented results only for real colour exposure. We have EEG signals belonging to three classes in our experiment to be classified as Red, Green and Blue and used ERSP data as features that was computed using EEGLAB (Delorme & Makeig 2004) Toolbox. We have ERSP datasets for each colour i.e. red, green and blue, for each subject. To acquire these datasets, ERSP was calculated for each trial in terms of time-frequency framework, for each colour among all the subjects. An average ERSP was taken across the trials for each colour as shown in figure 6 which represents the ERSP response for electrode position O2 across all the subjects for the real colours presented to the subjects. It is clearly visible in all the colours that variation in power in a specific frequency band at a certain time point is quite discriminative and remains discriminative for individual subjects for each colour. After the onset of stimuli, the highest increase in power is seen in red and lowest in blue during an interval from 100 to 400ms within delta and theta band. However, the lowest decrease in power is found in blue and highest in green during an interval from 250 to 1000ms within the alpha frequency band. These features were fed into SVM classifier.
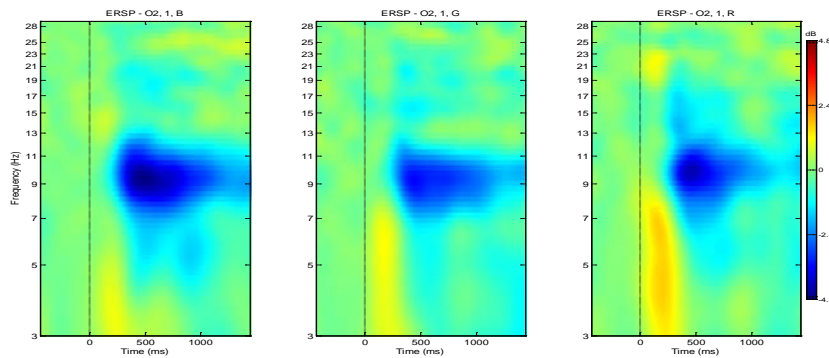

Figure 6. Averaged ERSP shown for electrode position O2. Right (Red), Middle (Green) and Left (Blue).

To classify EEG signals into red, green and blue classes, LIBSVM(Chang & Lin 2010)Toolbox was used which requires a specific format of data as follows in general,

 <Label Class1>   <index1> : <feature1> <index2> : <feature2> <index3> : <feature3> …

<Label Class2>   <index1> : <feature1> <index2> : <feature2> <index3> : <feature3> …

<Label Class3>   <index1> : <feature1> <index2> : <feature2> <index3> : <feature3> …

⋮   ⋮   ⋮   ⋮

Each row represents an instance or observation and each column represents the feature after the label column. Data was labeled before feeding to the classifier i.e. red labeled as 1, green labeled as 2 and blue labeled as 3. Numerically, ERSP data is present in two dimensional dataset of 100*200 values which indicate that there are 100 frequency points along rows and 200 time points along columns. For instance, to convert the data of subject 1 for channel P3, all the subject 1's colours i.e. red, green and blue are taken

into account and each time point along its frequency points is chosen randomly within a single colour and placed according to above format into the target dataset which will be used for training and testing of classifier. Once a time point is chosen from red class then a time point is chosen from green and finally from blue. This sequence continues until all the time points are chosen randomly within a single colour. Since there are 100 frequency points indicating 100 feature values in the target dataset against each label. Having three classes in hand, there would be 600 instances for data coming from channel P3, in the target dataset as each class contains 200 instances of time points i.e. each time point becomes an instance along the row in the target dataset with the corresponding label. After conversion, target dataset is divided into two subsets, one for training of classifier and the other is used for testing the classifier. As we have used four channels, two from parietal lobe and two from occipital lobe i.e. P3, P4, O1 and O2, the data was fed into the classifier not only as an individual channel but also in combination of different channels i.e. P3, P4, O1, O2, P3P4 (parietal region), O1O2(occipital region), P4O2(right occi-parietal), P3O1(left occi-parietal) and P3P4O1O2 (All). We have used C-SVC with linear kernel, polynomial kernel and RBF kernel where $\gamma = 0.1$ and degree of polynomial kernel is 3 along with default parameters. Tables 1, 2 and 3 present classification accuracies for linear, polynomial and RBF kernels respectively, for all the groups of data within all the subjects.

Table 1 presents the classification accuracies with an average accuracy of 84% for seven subjects among different groups of data which were used with linear kernel.

	S1	S2	S3	S4	S5	S6	S7
P3	90.74	83.7	85.19	85.93	84.82	84.82	81.85
P4	81.11	83.7	84.44	84.07	87.78	84.07	84.82
O1	81.11	86.3	81.85	84.82	88.15	82.96	87.78
O2	82.22	84.07	82.22	87.04	84.44	87.04	84.44
P3P4	83.7	85.93	83.89	87.41	88.15	84.63	84.44
O1O2	85	84.26	83.89	84.63	83.15	85.56	82.59
P4O2	85	82.78	83.89	84.26	85.93	85.93	82.59
P3O1	85	85.37	85.74	84.63	84.82	86.67	82.59
All	84.63	84.17	85	84.17	84.85	83.98	80.83

Table 2 presents the classification accuracies with an average accuracy of 89% for seven subjects among different groups of data which were used with polynomial kernel of degree 3.

	S1	S2	S3	S4	S5	S6	S7
P3	90	85.93	84.07	88.52	85.56	93.7	90.37
P4	83.7	86.67	86.3	89.63	91.11	89.63	91.85
O1	85.56	87.41	86.67	90.37	87.78	91.11	92.22
O2	83.7	86.67	89.25	87.04	86.3	87.78	88.15
P3P4	88.7	87.22	92.96	91.85	96.3	93.15	89.82
O1O2	85.74	82.59	81.48	88.33	90.56	87.41	89.07
P4O2	90.19	87.96	87.41	88.7	86.48	82.96	87.96
P3O1	87.41	84.63	84.26	92.22	90.56	92.96	87.78
All	92.59	90.74	88.89	91.57	95.56	89.17	87.41

Table 3 presents the classification accuracies with an average accuracy of 98% for seven subjects among different groups of data which were used with RBF kernel.

	S1	S2	S3	S4	S5	S6	S7
P3	99.63	96.3	99.26	96.67	97.04	97.41	99.63
P4	96.3	95.56	97.78	100	97.78	97.04	98.89
O1	94.82	96.3	95.93	99.63	97.04	96.67	98.15
O2	95.56	97.04	99.26	100	93.7	92.22	98.15
P3P4	97.78	94.63	99.63	99.82	100	99.44	97.78
O1O2	97.41	95	99.96	99.44	97.59	90.37	97.04
P4O2	98.33	93.7	99.3	99.3	96.85	95.93	97.59
P3O1	98.52	97.04	98.7	98.33	97.41	98.7	98.89
All	99.26	95.37	98.8	99.72	98.43	96.11	97.87

Classification accuracies for the data from all the channels (P3P4O1O2) with in all the subjects is shown in figure 7 for the three kernels used. Linear kernel has come up with lowest accuracy and RBF with highest accuracy in all the subjects. Similar results for the rest of the groups of data were also seen with an ascending order from lower to higher accuracy for linear, polynomial and RBF kernels in all the subjects. However, in some cases linear kernel has proven to be slightly better than polynomial in occipital region. Results regarding linear, polynomial and RBF kernels performances are shown in figures 7, 8 and 9 for data groups 'All', 'parietal' and 'occipital' channels respectively. However, the results for individual channels and right and left occi-parietal channels are similar. Tools used in this study are BCI2000 (Schalk et al. 2004), EEGLAB (Delorme & Makeig 2004) and LIBSVM (Hsu et al. 2003; Chang & Lin 2010; Fan et al. 2005).
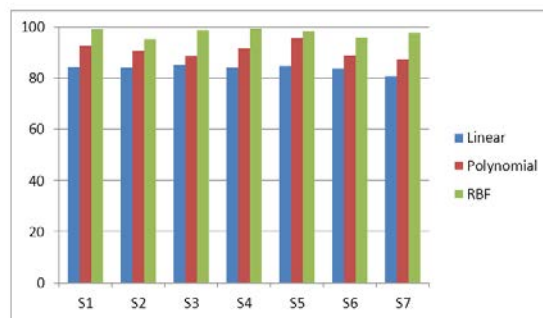

Figure 7. Classification accuracies in comparison among linear, polynomial and RBF kernels for data from all channels.
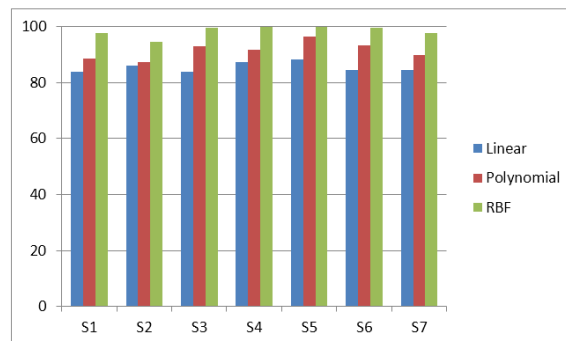

Figure 8. Classification accuracies in comparison among linear, polynomial and RBF kernels for data from parietal channels.
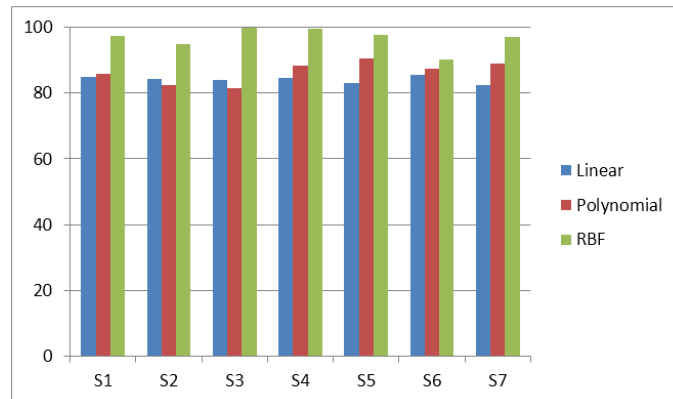
Figure 9. Classification accuracies in comparison among linear, polynomial and RBF kernels for data from occipital channels.

[51]**Conclusion**

In this experiment we presented only primary colours to the subjects in random sequence in order to have discriminative EEG signals from parietal and occipital regions of brain. We have used ERSP data as features and C-SVM as classifier with three different kernels i.e. linear kernel, polynomial kernel and RBF kernel for the classification of EEG signals recorded as event-related potentials in response to RGB uniform colour stimuli. To interpret more accurately the differences among the exposure of primary colours, average event related spectral perturbation (ERSP) results in terms of time-frequency frame are presented in figure 5, that have shown significant power variations in the delta, theta and alpha bands. Red exposure has shown highest power increase starting from 100 ms to 400 ms in delta and theta bands than green and blue exposures, however the blue exposure has the lowest increase in power within the same time period and frequency bands. Moreover, a discriminative decrease in power among all the colours is seen in alpha band within 1000ms after the onset of stimulus. We have seen that these differences against the visual conditions in terms of single uniform colours are successfully classified using support vector machine. We have found very good accuracy results, on average 84%, 89% and 98% for linear, polynomial and RBF kernels respectively, with in all the groups of data among all the subjects. Highest accuracy was found in RBF kernel with nowhere less than other kernels in any group of data in any subject. As a next step, we propose to do a comparative study on different classifiers in conjunction with dimensionality reduction to select the most suitable data features in order to eliminate redundant information.

REFERENCES

[1]   Abe, S., 2005. Support Vector Machines for Pattern Classification S. Singh, Japan: Springer.

[2]   Benjamin, B., Gabriel, C. & Müller, K., 2002. Classifying Single Trial EEG : Towards Brain Computer Interfacing. In Advances in Neural Inf. Proc. Systems. MIT Press, pp. 157--164.

[3]   Chang, C. & Lin, C., 2010. LIBSVM : a Library for Support Vector Machines. Department of Computer Science, National Taiwan University, Taiwan, 1-30.

[4]   Chiappa, S. & Barber, D., 2006. EEG classification using generative independent component analysis. Neurocomputing, 69, 769-777.

[5]   Delorme, A. & Makeig, S., 2004. EEGLAB : an open source toolbox for analysis of single-trial EEG dynamics including independent component analysis. Journal of Neuroscience Methods, 134, 9-21.

[6]   Dobelle, W.H., 2000. Artificial Vision for the Blind by Connecting a Television Camera to the Visual Cortex. ASAIO, 46, 3-9.

[7]   Fan, R., Chen, P. & Lin, C., 2005. Working Set Selection Using Second Order Information for Training Support Vector Machines. Journal of Machine Learning Research, 6, 1889-1918.

[8]   Farwell, L. & Donchin, E., 1988. Talking off the top of your head - Toward a mental prosthesis utilizing event-related brain potentials. Electroencephalography and Clinical Neurophysiology, 70(6), 510-523.

[9]   Foresta, F.L., Mammone, N. & Morabito, F.C., 2009. PCA – ICA for automatic identification of critical events in continuous coma-EEG monitoring. Biomedical Signal Processing And Control, 4(3), 229-235.

[10]   Garrett, D. et al., 2003. Comparison of Linear, Nonlinear, and Feature Selection Methods for EEG Signal Classification. IEEE Transactions on Neural Systems and Rehabilitation Engineering, 11(2), 141-144.

[11]   Guan, J. & Chen, Y., 2008. Single-trial EEG classification using in-phase average for brain-computer interface. Frontiers of Electrical and Electronic Engineering in China, 3(2), 194-197.

[12]   Hallez, H. et al., 2009. Removing muscle and eye artifacts using blind source separation techniques in ictal EEG source imaging. Clinical Neurophysiology, 120(7), 1262-1272.

[13]   Hsu, C., Chang, C. & Lin, C., 2003. A Practical Guide to Support Vector Classification, National Taiwan University.

[14] Huang, R., Jung, T. & Makeig, S., 2005. Analyzing Event-Related Brain Dynamics in Continuous Compensatory Tracking Tasks. In IEEE-EMBS 27th Annual International Conference of Engineering in Medicine and Biology. Shanghai, pp. 5750-5753.

[15] James, C.J. & Hesse, C.W., 2005. Independent component analysis for biomedical signals. Physiological Measurement, 26, R15-R39.

[16] Jung, T. et al., 2000. Independent Component Analysis of Biomedical Signals. In Proc. Int. Workshop on Independent Component Analysis and Signal Separation. pp. 633-644.

[17] Jung, T. et al., 2000. Removal of eye activity artifacts from visual event-related potentials in normal and clinical subjects. Clinical Neurophysiology, 111(10), 1745-1758.

[18] Kaper, M. et al., 2004. BCI Competition 2003 — Data Set IIb : Support Vector Machines for the P300 Speller Paradigm. IEEE Transactions on Biomedical Engineering, 51(6), 1073-1076.

[19] Krusienski, D.J. et al., 2008. Toward Enhanced P300 Speller Performance. Journal of Neuroscience Methods, 167(1), 15-21.

[20] Leeb, R. et al., 2006. Walking by Thinking : The Brainwaves Are Crucial , Not the Muscles ! PRESENCE, 15(5), 500 -514.

[21] Lotte, F. et al., 2007. A review of classification algorithms for EEG-based brain – computer interfaces. Journal of Neural Engineering, 4(2), R1-R13.

[22] Makeig, S. et al., 2004. Mining event-related brain dynamics. Trends in Cognitive Sciences, 8(5), 204-210.

[23] Makeig, S., 1993. Auditory Event-Related Dynamics of the EEG Spectrum and Effects of Exposure to Tones. Electroencephalography and Clinical Neurophysiology, 86(4), 283-293.

[24] Peterson, D.A. et al., 2005. Feature Selection and Blind Source Separation in an EEG-Based Brain-Computer Interface. EURASIP Journal on Applied Signal Processing, 19, 3128-3140.

[25] Pfurtscheller, G. & Neuper, C., 2001. Motor Imagery and Direct Brain – Computer Communication. In Proceedings of the IEEE. pp. 1123-1134.

[26] Pires, G., Castelo-branco, M. & Nunes, U., 2008. Visual P300-based BCI to steer a Wheelchair: a Bayesian Approach. In 30th Annual International IEEE EMBS conference. Vancouver, pp. 658-661.

[27] Rakotomamonjy, A. et al., 2005. Ensemble of SVMs for Improving Brain Computer Interface P300 Speller Performances. In Artificial Neural Networks: Biological Inspirations – ICANN. Berlin: Springer, pp. 45-50.

[28] Schalk, G. et al., 2004. BCI 2000 : A General-Purpose Brain-Computer Interface (BCI) System. IEEE transactions on Biomedical Engineering, 51(6), 1034-1043.

[29] Steinwart, I. & Christmann, A., 2008. Support Vector Machines M.Jordan, J. Kleinberg, & B. Scholkopf, New York: Springer.

[30] Stone, J.V., 2004. Independent Component Analysis: A Tutorial Introduction, MIT Press.

[31] Vapnik, V.N., 2000. The Nature of Statistical Learning Theory M. Jordan et al., Springer.

[32] Wang, L., 2005. Support Vector Machines: Theory and Applications J. Kacprzyk, Springer.

[33] Wolpaw, J.R. et al., 2002. Brain – computer interfaces for communication and control. Clinical Neurophysiology, 113, 767-791.

[34] Yoto, A. et al., 2007. Effects of Object Color Stimuli on Human Brain Activities in Perception and Attention Referred to EEG Alpha Band Response. Journal of Physiological Anthropology, 26(3), 373-379.